# HYBRID WAVEGUIDES AND HETERODYNE DETECTORS INTEGRATED OPTICS FOR 10 MICRON WAVELENGTHS

D. B. Anderson, et al

Rockwell International Corporation

Prepared for:

Naval Research Laboratory
Advanced Research Projects Agency

28 February 1975

# HIGH SPEED GaAs ELECTRONIC DEVICES FOR INTEGRATED OPTICS AND MICROWAVES

By

D. Anderson
D. August
J. C. Boyd
R. L. Davis
J. D. McMullen



February 28, 1975

Prepared for the Director, Naval Research Laboratory
Contract N00014-73-C-0297

15 February 1973 to 30 November 1974 - $209,900
Sponsored By
Advanced Research Projects Agency
ARPA Order #2327, Program Code 3D10



Approved for Public Release; Distribution Unlimited

Electronics Research Division
Rockwell International Corporation
3370 Miraloma Avenue
Anaheim, California 92803

Unclassified

SECURITY CLASSIFICATION OF THIS PAGE (When Data Entered)

| REPORT DOCUMENTATION PAGE | | READ INSTRUCTIONS BEFORE COMPLETING FORM |
|---|---|---|
| 1. REPORT NUMBER<br>C73-291/12/501 | 2. GOVT ACCESSION NO. | 3. RECIPIENT'S CATALOG NUMBER |
| 4. TITLE (and Subtitle)<br>Hybrid Waveguides and Heterodyne Detectors, Integrated Optics for 10 Micron Wavelengths | | 5. TYPE OF REPORT & PERIOD COVERED<br>Final Technical Report<br>2/15/73 - 11/30/74<br>6. PERFORMING ORG. REPORT NUMBER<br>C73-291.12/501 |
| 7. AUTHOR(s)<br>D. B. Anderson, R. R. August, J. T. Boyd, R. L. Davis, J. D. McMullen | | 8. CONTRACT OR GRANT NUMBER(s)<br>N00014-73-C-0297 |
| 9. PERFORMING ORGANIZATION NAME AND ADDRESS<br>Rockwell International Corporation<br>Electronics Research Division<br>3370 Miraloma; Anaheim, CA 92803 | | 10. PROGRAM ELEMENT, PROJECT, TASK AREA & WORK UNIT NUMBERS<br>ARPA Order #2327, Program Code 3D10 |
| 11. CONTROLLING OFFICE NAME AND ADDRESS<br>Advanced Research Projects Agency<br>1400 Wilson Boulevard<br>Arlington, VA 22209 | | 12. REPORT DATE<br>February 28, 1975<br>13. NUMBER OF PAGES<br>~~94~~ 87 |
| 14. MONITORING AGENCY NAME & ADDRESS(if different from Controlling Office)<br>Naval Research Laboratory<br>Washington, D. C. 20375 | | 15. SECURITY CLASS. (of this report)<br>Unclassified<br>15a. DECLASSIFICATION/DOWNGRADING SCHEDULE<br>None |

16. DISTRIBUTION STATEMENT (of this Report)

Approved for Public Release; Distribution Unlimited.



17. DISTRIBUTION STATEMENT (of the abstract entered in Block 20, if different from Report)

18. SUPPLEMENTARY NOTES

The views and conclusions contained in this document are those of the authors and should not be interpreted as necessarily representing the official policies either expressed or implied of the Advanced Research Projects Agency or the U. S. Government.

19. KEY WORDS (Continue on reverse side if necessary and identify by block number)

Traveling wave photoconductive heterodyne detector

20. ABSTRACT (Continue on reverse side if necessary and identify by block number)

The infrared integrated optics technology for use in the ten micron region of the spectrum has been developed as reported herein, comprising a traveling-wave photoconductive heterodyne detector as may be applied to $CO_2$ laser receiver systems. The initial phase of this effort (previously reported) has considered various infrared waveguide structures, materials and compatible processes, together with a hybrid approach to coupling between waveguides through the substrate. A companion effort has addressed traveling-wave electrooptic interactions for phase modulation and surface elastooptic interactions for a

DD FORM 1 JAN 73 1473 EDITION OF 1 NOV 65 IS OBSOLETE



Unclassified

SECURITY CLASSIFICATION OF THIS PAGE (When Data Entered)

frequency shifter all in an integrated optics format to complement the other functional requirements of $CO_2$ laser systems.

The effort reported herein specifically addresses extrinsic photoconduction in gold-doped, antimony-compensated germanium at 77°K in a rectangular waveguide structure and using a gallium-arsenide substrate. A traveling-wave structure is employed wherein the input infrared waveguide is phase matched with the output electrical signal transmission line which also serves as the bias electrodes. Both the slot and strip configuration of the output signal transmission line were investigated. The optimum transverse infrared waveguide dimensions are in the 10 - 100 micron range, while a traveling-wave interaction length on the order of 5 cm was employed.

An analysis of the traveling-wave heterodyne detector structure includes the waveguides and phase matching; carrier excitation, lifetime, and diffusion; and detector operation and performance. The analysis of the traveling-wave structure shows that its intrinsic circuit bandwidth extends through the microwave range.

The experimental demonstrated bandwidth of the traveling-wave detector is 1 GHz. The carrier lifetime of the photoconductive process minimized by Sb compensation becomes the bandwidth-limiting mechanism when the optical-electrical circuit constraints are removed by the traveling-wave concept. Experiments have demonstrated that the longer waveguide length increasing the absorption enhances the responsivity of Au-doped, Sb-compensated Ge in the wavelength regime corresponding to $CO_2$ lasers.

The heterodyne detector traveling-wave structure design is on a firm base; however, the materials-processing technology requiring specific dopants and concentration levels in a thin-film structure requires further effort to achieve reproducibility with reasonable yield.

# TABLE OF CONTENTS

# I. INTRODUCTION

## A. BACKGROUND

The performance of military weapon systems has been immeasurably enhanced by the development and application of the electronic integrated circuit art because it has provided the means to increase reliability and life with significantly less burden upon the limited systems resources (power, size, weight and cost), while simultaneously providing for an increased information-handling capacity. Currently, a corresponding development of an integrated optics technology is underway with the expectation of realizing some of the same benefits for optical communication and sensor systems.

It is now evident that the fiber and integrated optics technology will evolve into several forms for a variety of applications in both the near and far infrared regions of the spectrum. The telecommunication industry[1] is developing the ultralow loss fiber to couple a GaAs electroluminescent diode source to an Si photodetector as a first-generation incoherent multimode communications channel. It is the intent that the repeaters now requiring electronic amplification will eventually be replaced by an all-optical integrated circuit using coherent radiation and single-mode propagation as a second-generation ultrawide band communications system. Current DoD interest[2] in this fiber technology is largely motivated by its immunity to all types of environments rather than exploiting its potential ultrawide band communication capacity. Various intravehicular communication control systems have demonstrated the immunity to interference, corrosion, fire, vibration, fatique, electromagnetic pulse, crosstalk, and radio frequency interference. Glass fiber and interface semiconductor technology also represents a substantial saving of cost, size and weight over the current application of metallic conductors.

Some applications of optical integrated circuit technology cannot be constrained mechanically by the fiber but instead will employ small, highly collimated coherent optical beams. These systems will be largely concentrated in the far infrared, corresponding to efficient laser emission lines that are coordinated with the atmospheric "windows." Applications of these

free-space-bounded systems will include high resolution sensors and secure communication systems. The propagation path of these latter systems will traverse regions of limited "right of way," such as the presence of the enemy, terrain, ocean and space.

The integrated optics technology to complement the $CO_2$ laser technology is merited because the emission band occurs in the atmospheric window which is least affected meteorologically and because the $CO_2$ laser is capable of large power outputs realized efficiently. Aside from high-power $CO_2$ lasers, amplifiers and associated high-power transmitting optical elements for scanning, all other functions of communication and sensor systems are amenable to application of an integrated optics approach. These latter functions will be power-limited because of the macroscopic dimensions of the infrared waveguide. However, the attendent high fields lead to efficient interactions and when distributed yield ultrawide band characteristics. Thus, applications of far infrared integrated circuit technology will be confined to the receiver and associated signal processing (modulation functions).

The rotational-vibrational emission lines of the $CO_2$ laser extend over 20 percent of the infrared spectrum near ten microns. In addition, this laser may be operated at comparatively high pressure with collision broadened linewidths extending through the microwave into the millimeter spectrum. When $CO_2$ laser systems are employed to detect high velocity targets or are on high velocity vehicles, the resulting Doppler shift extends into the microwave region. Thus, heterodyne receivers for these systems must either have sufficient bandwidth to accommodate the Doppler offset or a local oscillator capable of tracking the Doppler shift. In coherent heterodyne systems where the local oscillator is derived by a frequency offset from the master oscillator, a variable frequency shifter is required so as not to compromise the sensitivity due to excessive bandwidth. This type of frequency shifter is amenable to an integrated optics approach.

Active $CO_2$ laser sensor systems can circumvent the limited peak power-handling capacity of infrared waveguides by employing a spread spectrum to increase the energy and match filter concepts for detection. These sensor systems requiring high range resolution and high data rate communication require wide band performance also extending into the microwave region.

The corresponding surveillance systems responsive to this technology must also have comparable bandwidth capability. Thus, the modulation function, both temporal and spatial, and the detection process must exhibit wide band and efficient transfer characteristics to exploit the $CO_2$ laser technology.

B. PROGRAM OBJECTIVE

This program has addressed several aspects in the development of a far infrared integrated optics technology to complement $CO_2$ laser systems. The initial effort was directed to the development of the passive waveguide components employing various heteroepitaxial structures and the coupling techniques to form a hybrid assembly.[3,4] Various aspects of materials, structures and processing were considered to identify a preferred set apposite to the far infrared. The current effort[5] reported herein addresses specifically the development of a traveling wave photoconductive heterodyne detector where wide base-band response is required to accommodate wide band signals with large Doppler offsets. This current effort has also considered the complementary accessories providing coupling to a telescope aperture and to a far infrared fiber.

Companion programs to complement this development of a far infrared integrated optics technology have considered the wide band temporal and spatial modulation functions[6] and the $CO_2$ local oscillator requirement,[7,8] all employing an integrated optics approach. Electro-optic and surface elasto-optic interactions were considered for these modulation functions with the latter being employed specifically to implement a frequency shifter such that, in combination with a master $CO_2$ laser, the local oscillator requirement is fulfilled for a coherent heterodyne receiver system. An underlying feature of each of these programs is the commonality of material-structures and the use of a Ge waveguide on a GaAs substrate.

C. APPROACH

The design considerations for a wide base-band heterodyne detector for coherent radiation differs substantially from detectors optimized for response to thermal radiation requiring wide spectral response and relatively narrow base bandwidth. Further, various other constraints have been imposed upon the design considerations for implementation of the heterodyne detector function in the far infrared in an integrated optics format. They include the infrared spectral response matched to the $CO_2$ laser, a wide signal base-

bandwidth, the requirement for a cryogenic environment at only 77°K, and the current availability of a suitable material-structure including the appropriate compatible processing techniques. All of these characteristics are intimately related to the detector material selected.

In the 10 micron region of the spectrum the extrinsic photoconductors responsive at 77°K include Te, Ge and Si with suitable dopants. Gold-doped Ge with Sb compensation for fast response has the most mature technology base. The corresponding intrinsic photovoltaic detectors responsive at 77°K include the narrow band gap ternary semiconductor compounds (HgCd)Te and (PbSn)Te. During the initial phase of this contract, photoconductive response in Au-doped Ge thin films and thin-film Schottky barrier (PbSn)Te diodes on $BaF_2$ were demonstrated using a linear-array strip geometry resembling waveguides.

Noise considerations show that the photovoltaic mode is advantageous over the photoconductive mode because of the lack of regeneration-recombination noise. The development of a stable planar processing technology for the ternary semiconductor compounds of interest is in an embryonic state. Because investigations of (PbSn)Te and (HgCd)Te are underway elsewhere, their consideration was de-emphasized in preference to extrinsic photoconductivity in a traveling-wave structure. Conventional Au-doped Ge photoconductive detectors exhibit a significant compromise of the responsivity in the spectral region corresponding to the $CO_2$ laser emission because of the low absorption. This has been overcome by using a comparatively long waveguide structure and which is phase-matched in a traveling-wave mode so as to prevent the structure from compromising the response time.

# II. TECHNICAL DISCUSSION

## A. TRAVELING-WAVE HETERODYNE DETECTOR DESIGN CONSIDERATIONS

The effort delineated and documented herein reports the design considerations in the development of a wide band traveling-wave heterodyne detector and the associated coupling employing an integrated optics format.

### 1. Detector Materials

Several criteria have lead to the selection of photoconductivity in extrinsic Ge. High-sensitivity detectors in the far infrared have required a cryogenic environment to suppress various sources of extraneous noise. Consideration has been restricted to a cryogenic environment obtained from liquid nitrogen as a means to minimize the impact upon system performance. Lower temperatures are to be avoided because of cost (Ne), hazard ($H_2$), complications of a double Dewar (He), availability and limited life.

The extrinsic photoconductors of interest in the ten micron region of the spectrum include Te, Ge and Si. Suitable dopants providing a response at 77°K include Sb, Au and In, respectively. The corresponding narrow band gap ternary semiconductor compounds which exhibit intrinsic absorption in the spectral region and function in the photovoltaic mode include (HgCd)Te and (PbSn)Te. Some characteristics of infrared detectors formed from these materials are summarized in Table I. Typical quantum efficiency and response time of discrete devices has been included. The corresponding representative spectral response is indicated in Figure 1.

Although a fast response has been obtained from a Te photoconductive detector, the high density of defects in thin-film depositions and the difficulties involved to control impurities have negated its consideration. Recent photoconductive detector developments have considered Si with various dopants. Two factors preclude its consideration. Silicon exhibits significant absorption bands near ten microns which prevents its use as an input coupling waveguide into the photoconductive waveguide section. Further, high deposition temperatures are necessary for epitaxy which introduces cross-doping from the substrate. Germanium, on the other hand, exhibits low absorption in the ten micron region and so may be used as the passive input coupling waveguide to the active photoconductive section. It also

TABLE I. INFRARED DETECTORS

| Material | Temperature °K | Spectral Response $\lambda$ ($\mu$) peak/$\lambda$ ($\mu$) ½cutoff | Absorption Coefficient $cm^{-1}$ | Quantum Efficiency | Response Time (sec.) |
|---|---|---|---|---|---|
| **PHOTOCONDUCTIVE** | | | | | |
| Ge: Au | 77 | 6/9 | ~2 @ 6$\mu$ | .2-.3 @ 6$\mu$ | $3\times10^{-8}$ |
| Ge: Au(Sb) | 77 | 6/9 | ~0.4 @ 10$\mu$ | .02 @ 10$\mu$ | $1.6\times10^{-9}$ |
| Ge: Hg | 28 | 11/14 | ~3 | .2-.6 @ 10$\mu$ | $2\times10^{-9}$ |
| Ge: Cu | 4.2 | 23/27 | ~4 | .2-.6 @ 20$\mu$ | $3\times10^{-9}$ |
| Si: In | 77 | 5.2/8.6 | | .6 @ 6$\mu$ | $1.5\times10^{-6}$ |
| **PHOTOVOLTAIC** | | | | | |
| PbSnTe | 77 | 10/12 | $\sim10^{4}$ | ~.6 @ 10$\mu$ | $1.5\times10^{-8}$ |
| HgCdTe | 77 | 10/12 | $\sim10^{3}$ | ~.6 @ 10$\mu$ | $\sim2\times10^{-7}$ |

requires a comparatively high temperature for thin-film depositions. However, various methods are available for investigation and which may be used with a GaAs substrate.

Noise considerations show that the photovoltaic mode is advantageous over the photoconductive mode because of the lack of regeneration-recombination noise. Good photovoltaic detector-diodes have been realized using the ternary semiconductor compounds (HgCd)Te and (PbSn)Te with the composition adjusted for the response in the ten micron region. The large intrinsic optical absorption requires that the diode approach microscopic dimensions to reduce the RC time constant and thus extend the high-frequency response. Currently, surface conditions and processing technology hamper the use of these materials for detectors in an integrated optics format. Because investigations of (PbSn)Te[9,11] and (HgCd)Te[12] are underway elsewhere, their consideration in this program was suppressed in preference to extrinsic photoconductivity in a Ge traveling-wave structure.

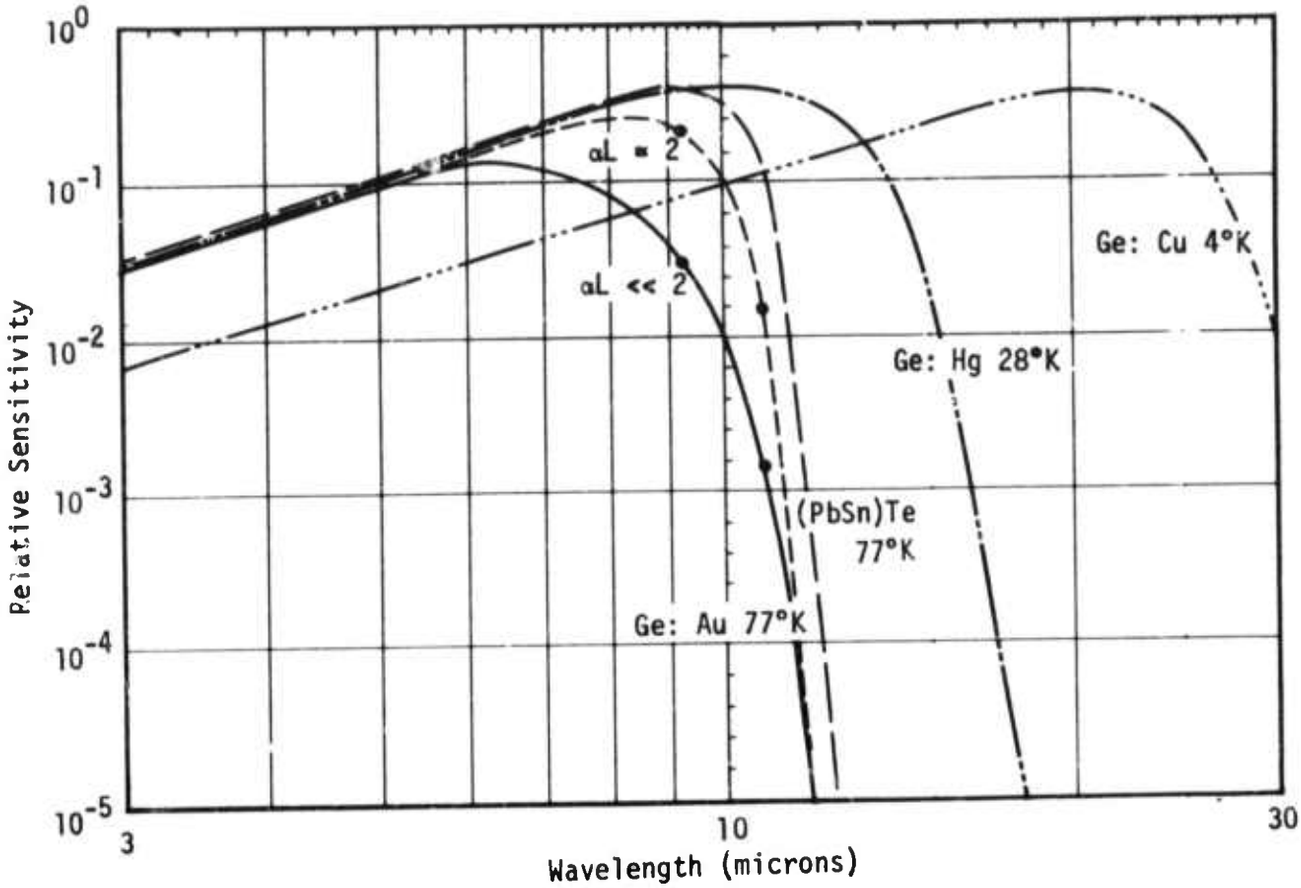


Figure 1. Representative Far Infrared Detector Spectral Response

An inspection of Table I shows that the quantum efficiency of typical bulk Au-doped Ge photoconductive detectors is comparatively low at ten microns because of the low absorption coefficient of Ge:Au and because of the limited detector dimensions. This leads to a maximum responsivity at a shorter wavelength, typically 6 microns. Further, gold is the only dopant providing a response near liquid nitrogen temperatures. To realize high quantum efficiency from Au-doped Ge requires a substantial increase of the absorption length, which, in a discrete element structure, will compromise the time response. The computed result of increasing the detector length of typical dimensions of several millimeters to several centimeters is indicated in Figure 1 by the shift from the solid to the dashed curve. To prevent a compromise of the detector time response, the traveling-wave concept is introduced, analyzed and applied in an integrated optics format.

## 2. Traveling-Wave Detector Structure

The traveling-wave concept applied to the heterodyne photoconductive detector considered herein is illustrated in Figure 2. The optical structure employes a Ge thin-film waveguide on a high-resistivity GaAs substrate as a rectangular dielectric image line. The optical signal and local oscillator signal as collinear free-space beams are coupled into the waveguide by way of a cylindrical immersion lens in optical contact with the Ge waveguide. The Ge waveguide with Sb compensation to obtain low absorption extends across the substrate. A portion of this waveguide is also doped with Au to the saturation level to provide transverse photoconductivity responsive to the applied infrared radiation. In the detector section the optical signals propagate along the dielectric waveguide located between metallic conductors forming a transmission line in intimate contact with the Au-doped Ge, Sb-compensated waveguide. This electrical signal transmission line used for the intermediate beat frequency detected output signal also provides the means for applying the bias associated with the photoconductive detector. Wide bandwidth is achieved in part by phase-matching of the optical input waveguide and the electrical output signal transmission line traveling in the same direction. A termination resistor is provided to match the electrical transmission line so as to prevent the existence of standing waves.

Figure 2 illustrates two types of intermediate-frequency transmission-line cross-sections coupled to the rectangular optical waveguide. They are identified as a "strip" line and a "slot" line. These electrical signal transmission lines provide different ranges of impedance and phase velocity due to the filling factor. Each of these transmission lines support the transverse electro-magnetic mode. The optical waveguide phase velocity is determined by its transverse dimensions, the kind and order of the mode excited, and the dielectrics employed. The effective bandwidth of the traveling wave structure is limited by the phase velocity mismatch to just that value for which the optical and electrical waves slip by $\lambda/4$. The limiting bandwidth ($\Delta f$) is given by

$$\Delta f = \frac{1}{4L_d} \left( \frac{1}{v_{p_e}} - \frac{1}{v_{p_o}} \right)^{-1} , \qquad (1)$$

Alternative Signal/Optical
Transmission Line Cross-Sections

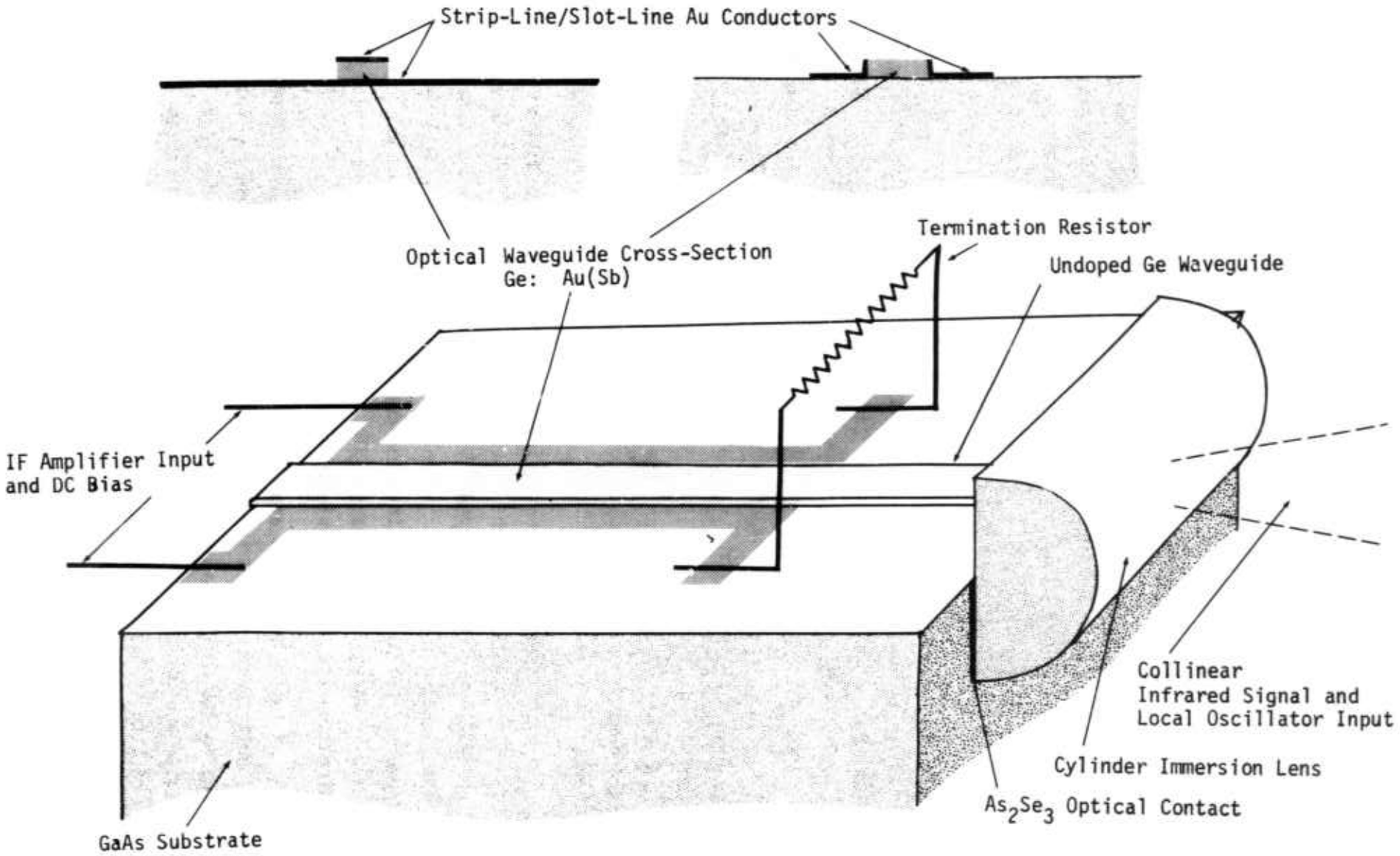


Figure 2. Traveling Wave Photoconductive Detector

where $L_d$ is the detector length and $v_{p_e}$ and $v_{p_o}$ are the phase velocity of the electrical and optical waves considered in a later section. When the optical waveguide and the detected output transmission line are phase-matched and impedance-matched, no circuit limitations are imposed upon the detector base-bandwidth.

There are two other requirements necessary to obtain high photoconductive gain and bandwidth; viz., reduced photoconductive transit time, which is obtained by the microscopic waveguide transverse dimensions and the minimization of the majority carrier (hole) lifetime obtained by compensation to achieve responsive heterodyne sensitivity.

A high quantum efficiency is achieved by employing a sufficiently long optical waveguide for an Au-doped Ge, Sb-compensated waveguide. The length must be on the order of several centimeters to absorb most of the radiation producing photo-induced carriers. The relative quantum efficiency of a discrete element Au-doped Ge photoconductive detector with Sb compensation and a traveling-wave structure as measured using a $CO_2$ laser is indicated in Figure 1. Obviously, the optical absorption contributing to the photoconductivity must exceed that due to the presence of the adjacent metallic output signal transmission line. Further, this imposes the requirement that the optical mode employed be restricted to the lowest order and of a quasi-transverse electric kind.

Heterodyne detection requires that the infrared signal and the local oscillator incident on the detector waveguide employ the same mode kind and order. These beams are usually combined with a beamsplitter taking most of the signal and reflecting a small portion of the excess local oscillator power prior to coupling into the detector such that the beams are collinear. A fully integrated approach could employ a parallel channel waveguide 10 dB directional coupler for single-ended operation.

A fully integrated approach in a balanced configuration using two detectors and hybrid junction is illustrated in Figure 3. This latter configuration can be used advantageously to suppress the local oscillator noise and minimize the local oscillator power requirements as is established practice in the microwave art. The balanced configuration illustrated in Figure 3 requires a similar hybrid junction in the input of

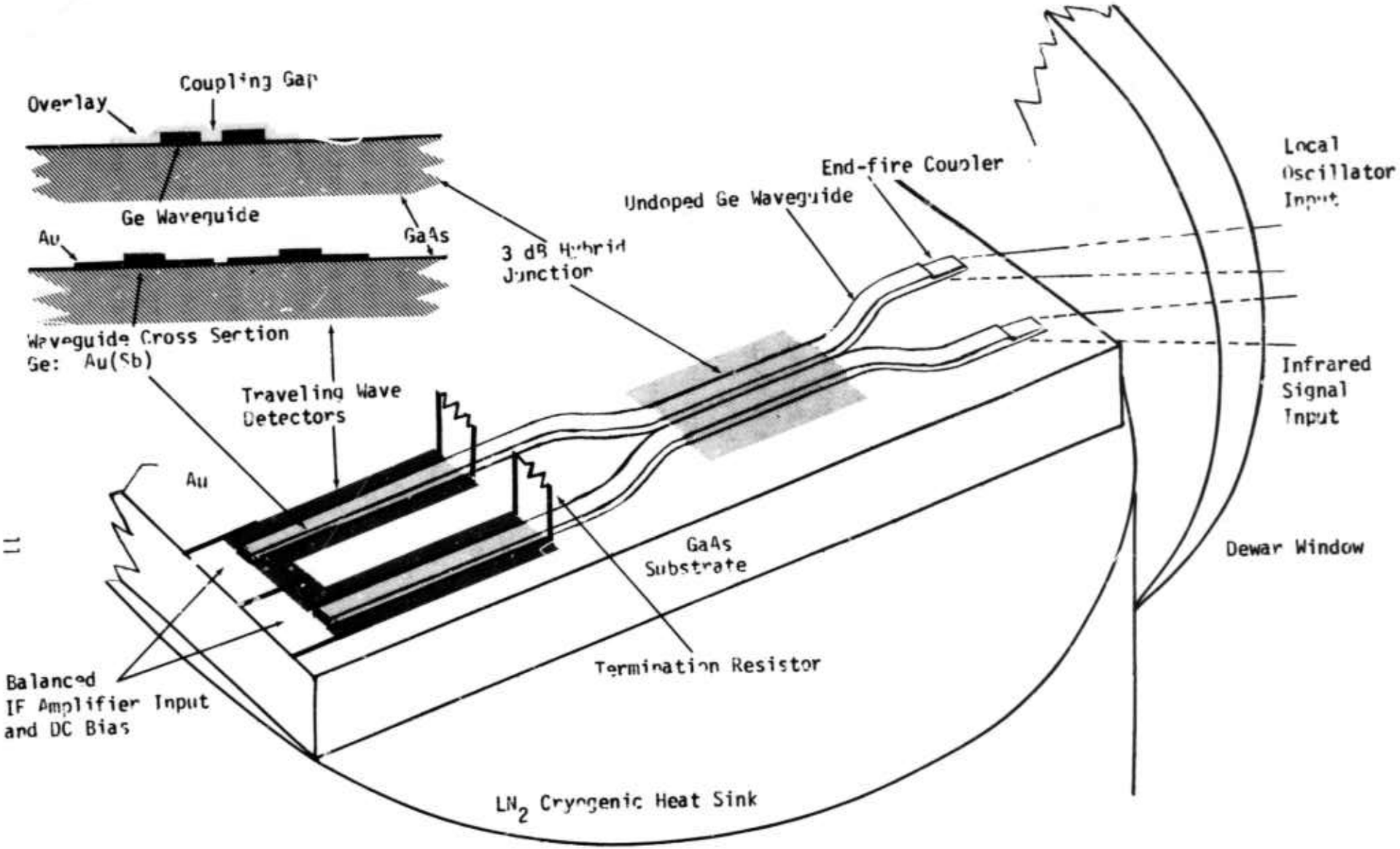


Figure 3. A Balanced Traveling-Wave Photoconductive Detector with Hybrid Junction Concept Illustrating an Integrated Optics Format

the IF amplifier. A central terminal for bias is indicated. End-fire couplers (taper) are illustrated in Figure 3. They may couple to other waveguide components following the hybrid concept, or to fibers, or to optical beams, all through the substrate. A backward wave grating is equally appropriate.

The slot-type transverse cross-section of the traveling-wave detectors is depicted in Figure 3. The transverse cross-section of the hybrid junction is also indicated. Both branches of the waveguide are brought sufficiently close together so that the evanescent fields from one waveguide are coupled to the other, producing equal division of the available power. Accurate adjustment of this coupling is achieved by a superstrate overlay in the coupling region such that the thickness of the superstrate filling the gap between the waveguides may be adjusted to control the coupling accurately. This process is done while the waveguides are in operation. The hybrid junction and traveling-wave detectors may be formed from a Ge thin film on a GaAs substrate. Gold represents the preferred material for the electrical network. All this structure must be mounted on a heat sink in a liquid nitrogen cryogenic Dewar. Inclusion of various circuit elements within the Dewar suppresses the background, arising from any waveguide absorption. Diffraction coupling is illustrated in Figure 3 through a side window.

The companion program[6] for the development of integrated optical modulators employs a GaAs waveguide on a (GaAl)As isolation layer on a GaAs substrate formed by vapor-phase epitaxy to create an electro-optic modulator. This program has also investigated a surface elastic wave Bragg-type frequency shifter employing GaAs as the piezoelectric substrate and Ge for the photo-elastic interaction region. Thus, either of these may be employed as a frequency shifter to convert a $CO_2$ laser master oscillator into a local oscillator for use with this receiver system. Either the electro-optic or the surface elasto-optic devices may also be incorporated into the Dewar and combined upon a single substrate with the hybrid junction and traveling-wave detector structure, providing full integration of a receiver.

A constraint of this effort as well as the companion effort has been the use of a compatible material-structure and processing sequence for the potential realization of full integration. Both the traveling-wave detector

hybrid junction and a potential frequency shifter require substrate dimensions and interaction lengths on the order of 5 centimeters. Such a large dimension of substrate and photolithographically defined patterns requiring micron resolution is at the threshold of the art, where yield becomes a critical parameter. The corresponding electronic integrated circuit art does employ silicon substrates with these dimensions and resolution requirements, however, with repetitious patterns achieved by step-and-repeat. Whereas, the optical integrated circuit as considered herein requires continuous, uninterrupted perfection throughout the entire device length, extending over the entire substrate. The consequences of the yield have forced the creation of patterns as arrays in order to assure a useful operating device.

The device structures investigated for the traveling-wave heterodyne detector have been restricted to the structural configuration illustrated in Figure 2. The traveling-wave heterodyne detector waveguide has been arranged as a linear parallel array providing for investigation of both the strip and slot signal transmission line cross-sections. Various processing means to realize the waveguide and substrate with and without Au doping and Sb compensation have been investigated. Macroscopic rectangular bars have also been prepared to demonstrate the traveling-wave concept independent of the processing employed to realize thin-film structures.

## 3. Optical Thin-Film Waveguides and Phase-Matching

To provide a basis for the discussion of the traveling wave photoconductive heterodyne detector we will summarize some of the properties of bound modes in dielectric waveguides. The waveguide structure considered is illustrated in Figure 4, which shows an infinite planar dielectric film supported by a dielectric substrate. The infinite planar dielectric film is considered because of the mathematical simplicity. The problems encountered with a rectangular cross-section have been treated elsewhere.[13-15] The use of the infinite planar approach is valid when the rectangular cross section aspect ratio exceeds five.

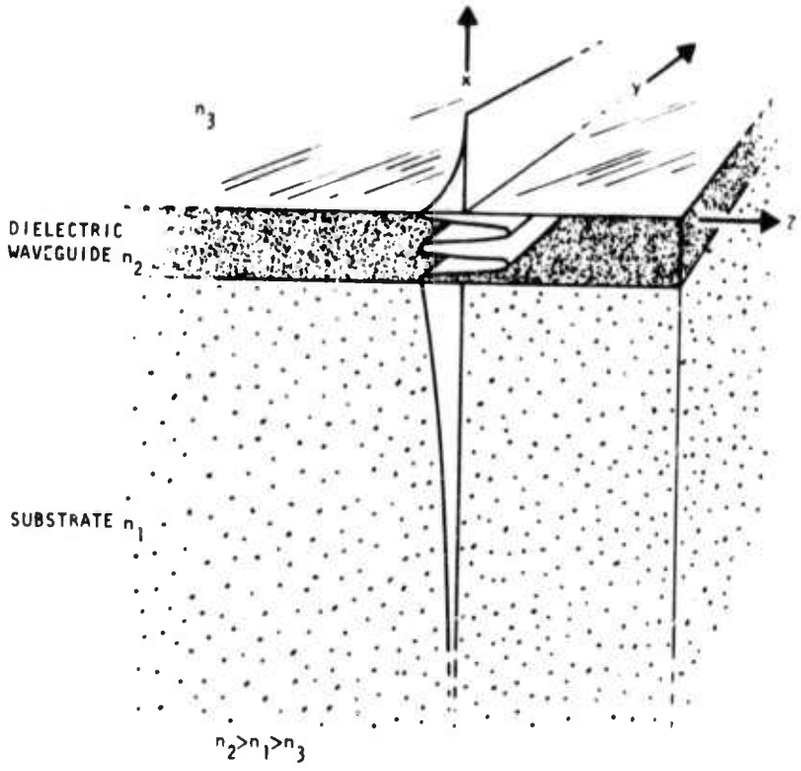


Figure 4. Cross-section of Asymmetrical Planar Dielectric Waveguide Showing Fourth Order Mode with Evanescent Field

To determine the properties of the dielectric waveguide modes, the electromagnetic wave equation must be solved subject to the boundary conditions that the tangential components of the electric and magnetic fields are continuous at the two boundaries $x = 0$ and $x = d$. By using

the z-dependence and the time dependence of the fields to be of the form:

$$e^{i(\omega t - \beta z)}$$

where $\omega$ is the angular frequency and $\beta$ the waveguide propagation constant, the field problem becomes a one-dimensional classical boundary value problem.

Solutions of this boundary value problem provide the transverse functional form of the fields according to:

$$\psi_1 = C\, e^{qx} \qquad x \leq 0 \qquad (2a)$$

$$\psi_2 = C \left[\cos(hx) + (q/h) \sin(hx)\right] \qquad 0 \leq x \leq d \qquad (2b)$$

$$\psi_3 = C \left[\cos(hd) + (q/h) \sin(hd)\right] e^{-p(x-d)} \qquad x \geq d \qquad (2c)$$

for TE modes where C is a normalization constant, q, h, and p are transverse components of the propagation vector in regions 1, 2, and 3, respectively. In Equation (2) we have used the coordinate system of Figure 4 and taken x=0 at the interface between regions 1 and 2. The thickness of the waveguide region 2 is d. The various propagation constants and d satisfy the waveguide dispersion relation:

$$\tan hd = \frac{h(q+p)}{h^2 - pq} \qquad (3)$$

As the waveguide fields in Equation (2) satisfy the wave equation, the propagation constants are related according to:

$$h^2 + \beta^2 = k^2 n_2^2 \qquad (4a)$$

$$-q^2 + \beta^2 = k^2 n_1^2 \qquad (4b)$$

$$-p^2 + \beta^2 = k^2 n_3^2 \qquad (4c)$$

In Equation (4), $k = 2\pi/\lambda$, where $\lambda$ is the optical wavelength and $n_1$, $n_2$, and $n_3$ are the refractive indices of regions 1, 2, and 3 in Figure 4. We let m = 0, 1, 2, 3 . . . M denote the mode order corresponding to the m-th eigenvalue of Equation (3). A typical field distribution corresponding to (2) for a three-layered waveguide structure is shown in Figure 5 up to the second order.

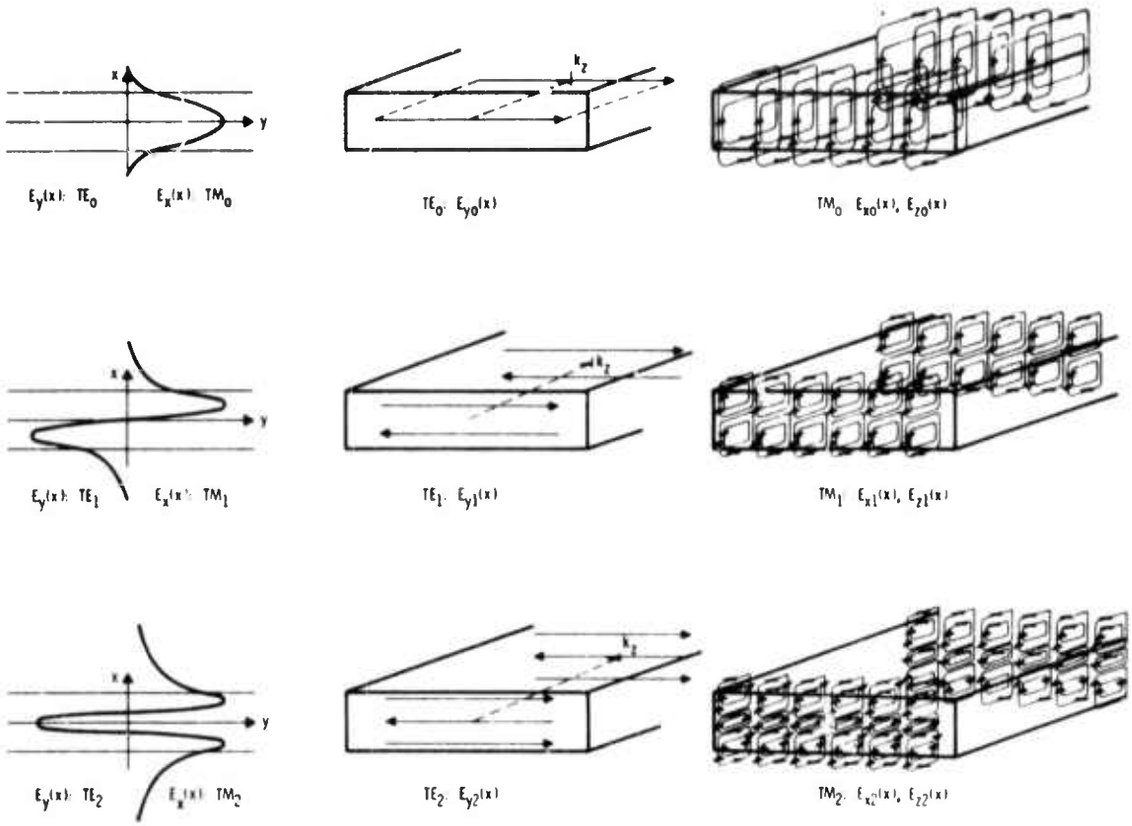


Figure 5. Dielectric Waveguide Field Distributions

It is convenient to define an effective refractive index $N_{eff}$ of a waveguide mode as:

$$N_{eff} = c/v_p = \beta/k, \tag{5}$$

where $v_p$ is the phase velocity of the waveguide mode. Values of $N_{eff}$ must lie in the range:

$$n_1 < N_{eff} < n_2 \tag{6}$$

where we assumed $n_1 \geq n_3$. The value of the effective refractive index for

a planar dielectric waveguide can be determined by solving the transcendental equation (3) numerically. The effective refractive index is a multivalued function of the frequency and waveguide thickness. A discrete effective refractive index exists for each bound propagating mode for all orders and kinds. The results for a Ge-on-GaAs structure considered herein are shown in Figure 6. The corresponding refractive index bounds are 4.0 on 3.3. It should be noted that all of the modes exhibit a cutoff including m = 0 because of the asymmetrical structure; i.e. $n_1 \neq n_3$. In the case of dielectric waveguides, the cutoff means that the wave is no longer bound to the high refractive index core but is allowed to leak into the cladding and/or substrate. Inspection of Figures 6 shows that the Ge thin film should be approximately three microns thick in order to limit the waveguide to the lowest order mode in the ten micron region.

This simple calculation and the dispersion results are strictly applicable to the infinite planar film on a substrate; whereas, practical waveguides are limited in extent to preserve field confinement throughout the propagation path in the thin film. In some devices field containment is achieved by diffraction of the source leading to a narrow collimated beam. When the dielectric thin film is limited in extent to form a rectangular dielectric waveguide (image line), the width dimension also becomes a control of the dispersion. The above infinite planar dielectric film leads to pure transverse electric and transverse magnetic modes; whereas, the rectangular dielectric waveguide leads to hybrid modes which are quasi-TE and quasi-TM when the rectangular cross-section aspect ratio is substantially other than unity. The electric field components of both transverse electric and transverse magnetic for orders 0, 1, and 2 are illustrated in Figure 5. The electric field orientation and configuration is also shown. Note that the extension of the evanescent field outside the dielectric boundaries increases as the mode order increases. In other words, the lowest order mode has the highest degree of wave binding. Figure 5 also applies to the magnetic field components by interchanging all electric and magnetic nomenclature. It should be noted that the rectangular dielectric waveguide cross-section leads to both longitudinal electric and magnetic components as well as transverse components, and, therefore, the use of the quasi-TE and quasi-TM nomenclature.

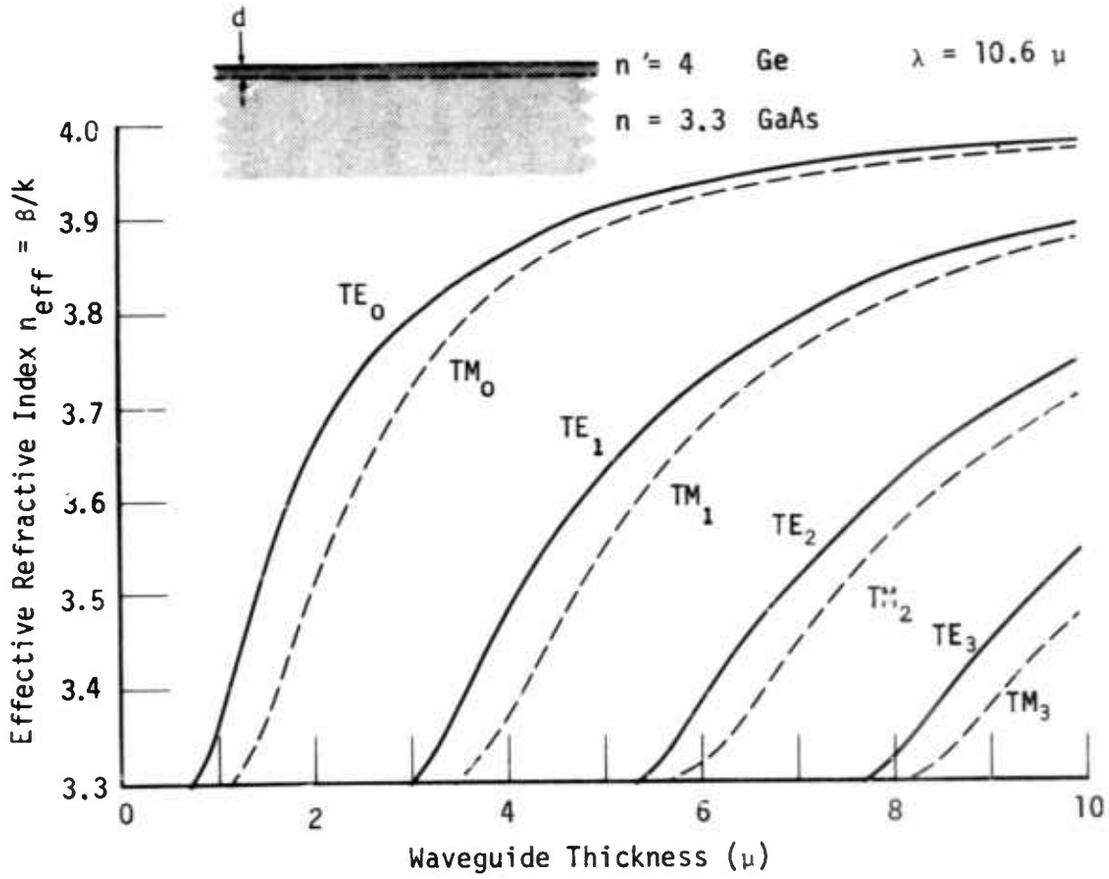


Figure 6. Dispersion of Ge Waveguide on GaAs Substrate as a Function of Thin-Film Thickness

For the traveling-wave heterodyne detector the electrical demodulated signal wave and both the optical waves (infrared signal and local oscillator) should travel at the same velocity to achieve wide base-band demodulation; i.e., phase-matched. The limiting detector bandwidth was given in Equation (1) in terms of the phase velocities. The phase velocities of the infrared signal and local oscillator in the optical waveguide are essentially equal. The phase velocity of the infrared signals and the electrical demodulated wave depend upon their respective waveguide structures. For an infrared wave propagating in a rectangular dielectric image line on a substrate with a superstrate, the phase velocity lies in the range

$$\frac{c}{n_2} < v_{p_o} < \frac{c}{n_1} < \frac{c}{n_3} \tag{7}$$

or as depicted in Figure 6. The electrical demodulated signal transmission line depicted in Figure 2 supports the TEM mode for either the strip or slot configuration. If the two-conductor transmission line is fully embedded in a homogeneous dielectric, the phase velocity is given as

$$v_{p_e} = c/\sqrt{\varepsilon_r} \quad , \tag{8}$$

where $\varepsilon_r$ is the relative dielectric constant. For Ge, $n_1 = 4.0$ and $\varepsilon_r = 16$ for infrared and microwave spectral regions of interest. The transmission lines illustrated in Figure 2 are only partially dielectrically filled and thus the effective phase velocity is greater than that given by Equation (8). The characteristic impedance of both the strip and slot cross-sections,[16] together with the corresponding effective refractive index are depicted in Figure 7, where the indicated dielectric is Ge. Typical dimensions for the strip transmission line lead to a substantially lower characteristic impedance in comparison with the slot. Whereas the strip transmission line exhibits a greater effective refractive index than the slot due to a larger filling factor; i.e., dielectric in the high field region. Application of a superstrate over the slot is a practial method to increase the effective refractive index (reduce $v_{p_e}$). Wide base-band demodulation requires that the "slot" or "strip" $v_{p_e}$ be matched to that of the optical waveguide $v_{p_o}$ shown in Figures

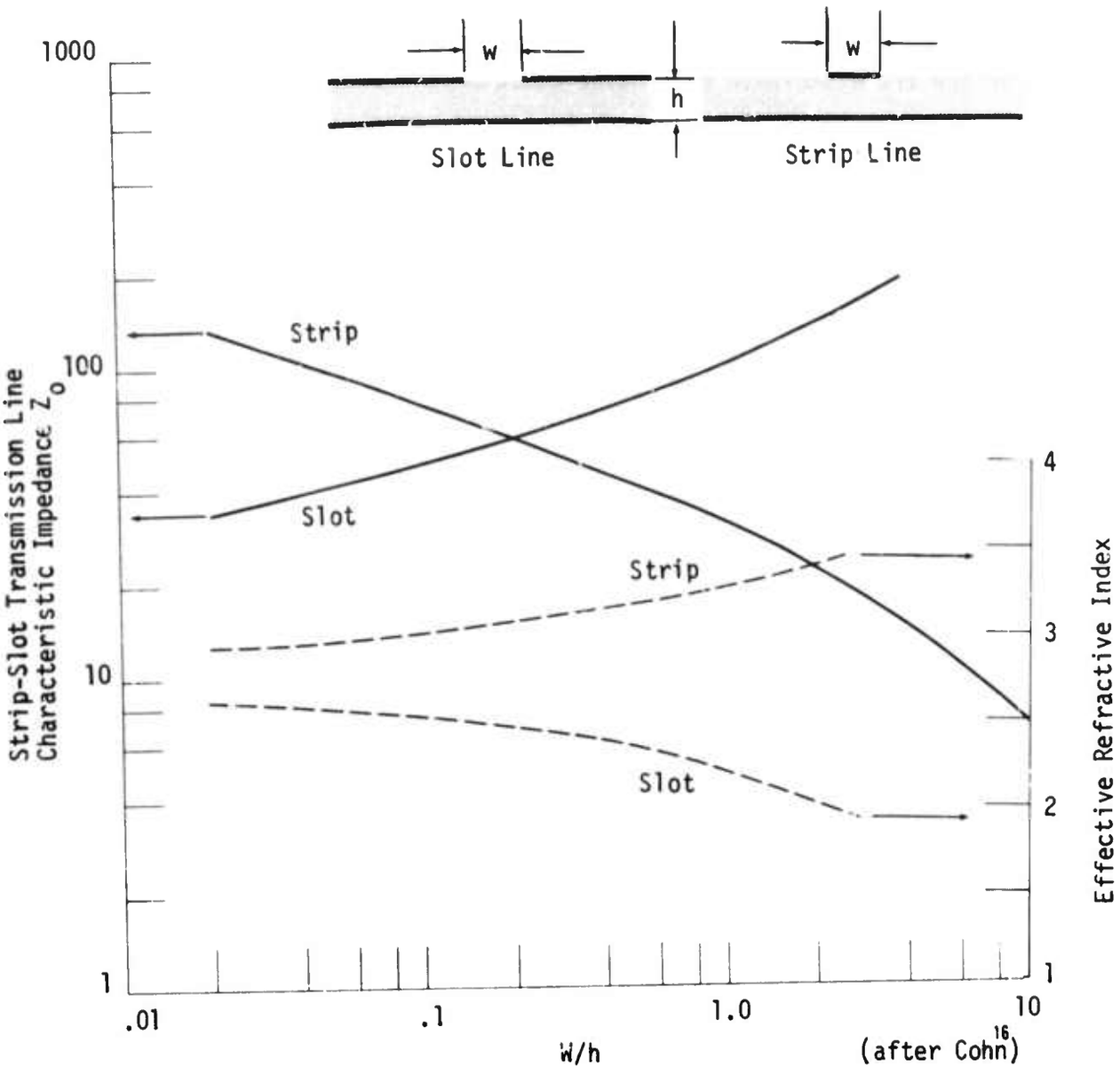


Figure 7. Characteristic Impedance of Strip and Slot Transmission Line and Effective Phase Velocity for GaAs Substrate

6 and 7. Rearranging Equation (1) employing the effective refractive index ($n_{eff}$) of each mode of propagation (optical and electrical), it becomes

$$\Delta f = \frac{c}{4L_d} \left( n_{eff_e} - n_{eff_o} \right)^{-1} \qquad (9)$$

For a lumped-element detector 4 cm long without phase matching $\left( n_{eff_o} \rightarrow 3.5, \; n_{eff_e} \rightarrow \infty \right)$, the limiting bandwidth $\Delta f$ becomes approximately .54 GHz.

If a traveling-wave structure is composed of a Ge film 3 microns thick on a GaAs substrate, from Figure 6 $n_{eff_o} \rightarrow 3.8$; and if a strip line electrode is employed 9 microns wide, the effective refractive index from Figure 7 $n_{eff_e} \rightarrow 3.5$. Then, from Equation (9) the limiting bandwidth becomes approximately 6 GHz. If the slot configuration is employed instead $n_{eff_e} \rightarrow 1.9$, the limiting bandwidth becomes 0.98 GHz. If the optical waveguide thickness is reduced to approximately 1.4 microns $n_{eff_o} \rightarrow 3.5$ and a strip transmission line is employed, $W/h \rightarrow 3$ so that $n_{eff_e} \rightarrow 3.5$. Then, phase mismatch is achieved and the traveling-wave structure places no limit upon the detector bandwidth.

Clearly, the strip configuration is preferred over the slot because it more closely matches the range of phase velocities in Equation (7). The strip line exhibits a comparatively low impedance; however, it is substantially less than that of the slot, where $W/h > 3$. When the phase-matching considerations are fulfilled, the intermediate frequency amplifier impedance matching and noise considerations will dictate the type of transmission line. The bandwidth differences of these two structures arises largely from the differences of the dielectr. filling factor.

## 4. Carrier Excitation and Diffusion

The effect of carrier diffusion in the direction of line propagation and the resulting bandwidth limitations are considered herein. The incident optical wave propagates in an optical waveguide (Ge) mode, while an electrical wave propagates collinearly along the transmission line formed by the gold electrodes. By utilizing an electrical wave traveling phase matched with the optical wave, a long detector length can be used without the structure sacrificing detector time response. A long detector length allows full absorption of the optical energy and thus leads to high quantum efficiency. For gold-doped germanium at $\lambda = 10.6\mu m$ we require detector length L to be greater than the absorption length $\alpha^{-1}$, i.e.,

$$L > \alpha^{-1} ,$$

then the transit time of the light propagating along the detector will be > .33 nsec. This value is the same order of magnitude as the desired time response of the detector. Normally, to achieve this response time for a photoconductive detector, w is made significantly less than $\alpha^{-1}$ thus sacrificing quantum efficiency, particularly for Au-doped Ge detector.

Over the long detector length the incident light induces a non-uniform distribution of excited carriers. There is thus some diffusion of excited carriers along the direction of light propagation. As this diffusion of carriers tends to smear out the electrical information extracted from the optical wave, we carefully analyze the extent of this diffusion. For the Ge detector in question, we find that this degradation of the electrical signal is not significant for frequencies $<10^{12}$ Hz.

To begin our analysis of carrier diffusion we must specify the nature of the field exciting the carriers. For heterodyne detection the total optical electric field E incident on the detector is the sum of a local oscillator field $E_L(z,t)$ and a signal field $E_S(z,t)$, i.e.,

$$E = E_L(z,t) + E_S(z,t), \tag{10}$$

where

$$E_L(z,t) = E_L\, e^{i(\omega_L t - k_L z)} + c.c \qquad (11\,a)$$

$$E_S(z,t) = E_S\, e^{i(\omega_S t - k_S z)} + c.c \qquad (11\,b)$$

and c.c indicates the complex conjugate. The propagation direction is taken as the z direction, $\omega_L$, $\omega_S$, $k_L$, and $k_S$ are the local oscillator and signal angular frequencies and propagation constants, respectively. The optical power $P_o(z,t)$ entering the detector is

$$P_o(z,t) = 4\,|E|^2\, A/Z_o$$

$$= r[E_L^2 + E_S^2 + 2\,E_L E_S \cos(\omega t - hz)]\, A/Z_o, \qquad (12)$$

where A is the waveguide cross sectional area, r is the fraction of the incident field coupled into the Ge waveguide, $Z_o = 377/n$ is the optical wave impedance of the waveguide detector, n is the waveguide refractive index, and

$$\omega = \omega_L - \omega_S \qquad (13a)$$

$$h = k_L - k_S \qquad (13b)$$

In determining (12) we assumed $E_L$ and $E_S$ real. The number of photons absorbed per second per $cm^3$, $N(z,t)$, in the Ge optical waveguide is distributed along the z direction according to

$$N(z,t) = \frac{\alpha}{\hbar\omega_L A}\, P_o(z,t)\, e^{-\alpha z}, \qquad (14)$$

where $\alpha$ is the absorption coefficient of the Ge waveguide and $\hbar$ is Planck's constant divided by $2\pi$. In arriving at (14) we assumed the signal and local oscillator photon energies to be equal, i.e., $\omega_L \approx \omega_S$. Substituting (12) into (14) we find that $N(z,t)$ has the form

$$N(z,t) = a\, e^{-\alpha z} + b\, e^{-\alpha z} \cos(\omega t - hz), \qquad (15)$$

where a and b are constants given as

$$a = \frac{rE_L^2\alpha}{Z_0\hbar\omega_L}, \quad E_L^2 >> E_S^2 \tag{16a}$$

$$b = \frac{2rE_LE_S\alpha}{Z_0\hbar\omega_L}. \tag{16b}$$

As each photon absorbed excites a hole, N(z,t) can also be interpreted as the hole concentration generation rate.

Equation (15) gives the rate at which the excess hole concentration is generated as a function of z and t. Holes are also recombining and diffusing along the z direction. The resultant excess hole concentration p(z,t) satisfies the diffusion equation[17]

$$D\frac{\partial^2 p}{\partial Z^2} - \frac{p}{\tau} + N(z,t) = \frac{\partial p}{\partial t}, \tag{17}$$

where $\tau$ is the hole recombination lifetime and D is the ambipolar diffusion constant.[18,19] As the solution of (17) with N(z,t) specified by (15) is quite involved, we consider first the steady state solution with a local oscillator field present, but with no signal field present. The constant b in (15) is thus zero. Assuming surface recombination is absent, the steady-state solution of (17) is

$$p(z,t) = \frac{\alpha a L_d(1/L_d^2 - \alpha^2)^{-1}}{2D\sinh(L/L_d)}\left[\left(e^{-\alpha L} - e^{-L/L_d}\right)e^{z/L_d} + \left(e^{-\alpha L} - e^{L/L_d)}\right)e^{-z/L_d}\right] + \frac{\alpha e^{-\alpha z}}{D(1/L_d^2 - \alpha^2)} \tag{18}$$

(zero signal)

In (18) $L_d$ is the diffusion length defined by

$$L_d = \sqrt{D\tau} \qquad (19)$$

For Ge:Au the hole diffusion length is plotted in Figure 8 as a function of $\tau$ for T = 77°. We see from Figure 8 that for the range of lifetimes of interest ($\tau < 10^{-7}$),

$$\alpha L_d \ll 1 , \qquad (20)$$

because $\alpha = .4cm^{-1}$ for Ge:Au. We also note that for detector lengths of interest $L > \alpha^{-1}$ so that

$$L \gg L_d . \qquad (21)$$

Using the inequalities (20) we can accurately approximate (18) as

$$p(z,t) = \tau a e^{-\alpha z} . \quad \text{(zero signal)} \qquad (22)$$

Thus, if conditions (20 and 21) are satisfied, the excited carrier concentration will have the same z dependence as the optical power in the detector material. The carrier concentration as a function of z is thus a true measure of the optical power provided the inequalities (20 and 21) are satisfied.

We now consider the presence of a signal. The rate of carrier excitation N(z,t) is now given by (15) with both a and b nonzero. For this situation, the solution to (17) can be found and again making use of the inequalities (20 and 21) this solution can be approximated as

$$p(z,t) = \tau a e^{-\alpha z} + \frac{\tau b e^{-\alpha z} \cos(\omega t - hz - \phi)}{\sqrt{(1+h^2 L_d^2)^2 + \omega^2 \tau^2}} , \qquad (23)$$

where

$$\tan \phi = \frac{\omega \tau}{1+h^2 L_d^2} . \qquad (24)$$

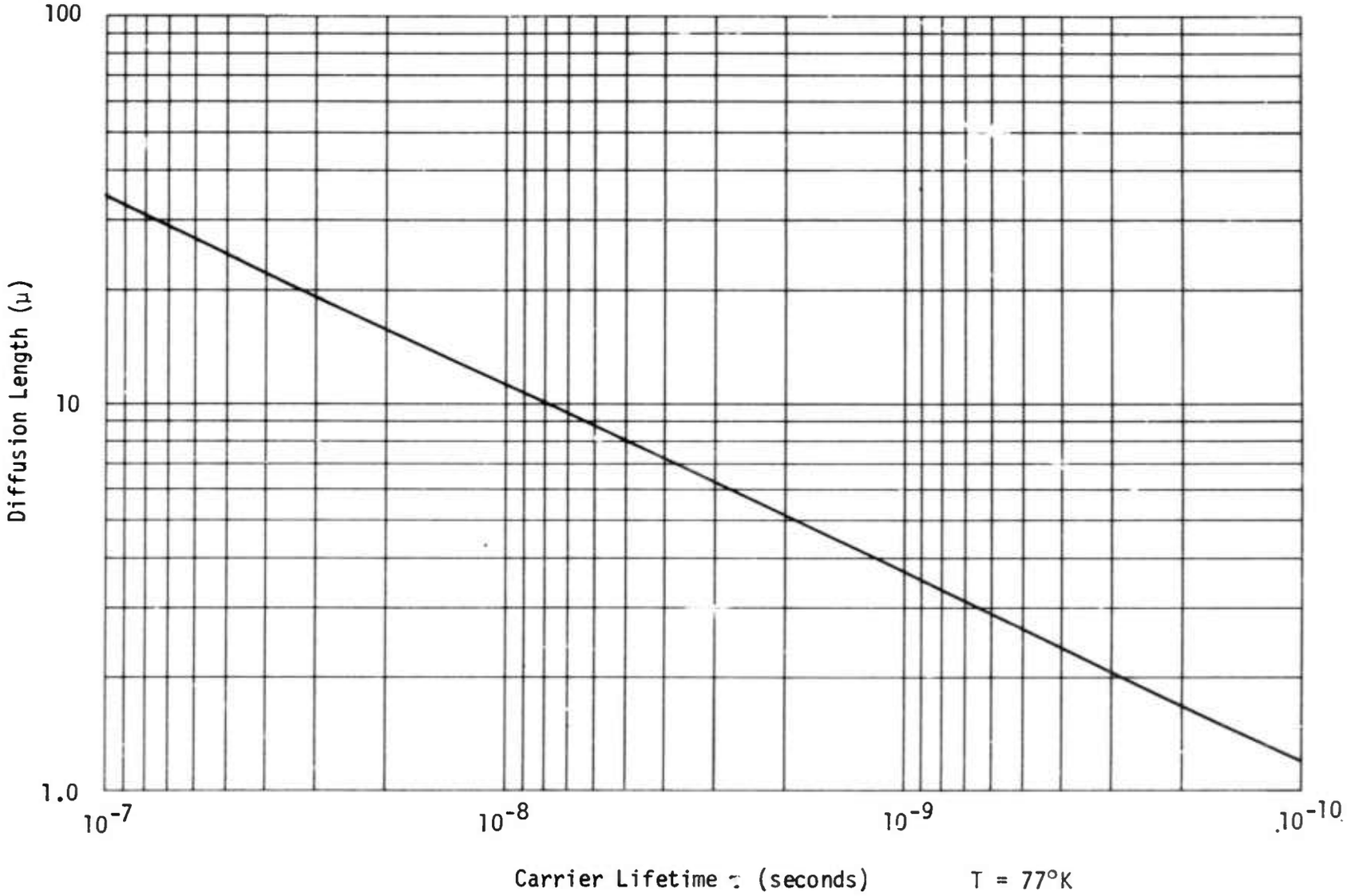


Figure 8. Hole Diffusion Length as a Function of Carrier Lifetime for Au Doped Ge

The square root term in the denominator of the second term in ( 23) describes the frequency response of the excited carrier concentration as $\omega$ increases. From this analysis, the detector signal voltage is proportional to the excited carrier concentration and thus, will have the same frequency response as the excited carrier concentration given by ( 23). We see from ( 23) that the detector frequency response will begin to fall off as $\omega$ increases when

$$\omega\tau \rightarrow 1 \tag{25a}$$

or when

$$(hL_d)^2 = (n \frac{\omega}{c} L_d)^2 \longrightarrow 1 \ . \tag{25b}$$

The first condition (25a) corresponds to the usual photoconductive lifetime limitation, while (25b) represents the limitations imposed by carrier diffusion in the z direction. This latter limitation is unique to the traveling wave detector. To avoid signal roll-off due to this diffusion limitation

$$hL_d < 1 \tag{26a}$$

which implies that

$$L_d < \frac{\lambda_e}{2\pi n} \ , \tag{26b}$$

where $\lambda_e$ is the electrical wavelength. The condition (26b) says that the average carrier diffusion length should be significantly less than the electrical half wavelength in order to avoid signal degradation. The condition (26a) limits our heterodyne frequency $f = \omega/2\pi$ to a value

$$f < \frac{c}{2\pi n L_d} \ , \tag{26c}$$

which, for Ge:Au with $\tau = 10^{-8}$

$$f < 9.18 \times 10^{11} \text{ Hz.}$$

In practice we thus expect that for Ge:Au the lifetime limitation (25a) will cause roll-off of the frequency response of the excited carrier concentration at much lower frequency than the diffusion limitation (25b).

A phase shift $\phi$ defined in (24) accompanies the degradation of the frequency response as $\omega\tau \rightarrow 1$. But note that the effects of diffusion as $bL_d \rightarrow 1$ cause this phase shift to be reduced. We can account for this by considering the physical effect of diffusion, i.e., to induce carrier movement in the $+z$ direction. This carrier movement tends to compensate for the phase retardation which occurs as $\omega\tau \rightarrow 1$.

In (19) we detailed the limitation of diffusion on the traveling wave detector frequency response. We should emphasize that for the traveling wave detector output signal to be a true measure of the incident light intensity, the conditions (20 and 21) restricting the diffusion length must be satisfied. When these conditions are satisfied, (23) the output signal accurately represents the induced carrier concentration. As noted earlier, for lifetimes of interest, the diffusion length in Ge:Au at 77° easily satisfies the conditions (20 and 21).

From a device point of view, the response of a photodetector is limited by the characteristic time in which excited carriers contribute to the current flowing through the photodetector.[20] We shall refer to this characteristic time as the device carrier lifetime. For a photoconductive detector in which the excited carriers are instantaneously replenished once they reach an electrode, the device carrier lifetime is equal to the carrier recombination lifetime.[21] Like the conventional photoconductive detector, the traveling wave photoconductive detector allows such replenishment of excited carriers once they reach an electrode. The device carrier lifetime of a traveling wave detector is thus equal to the carrier recombination lifetime. This behavior contrasts with that of the photodiode in which excited

carriers are not replenished and, as a consequence, the device carrier lifetime is equal to the transit time of the excited carriers moving from one side of the p-n junction to the other.[20,21]

The analysis thus far assumes that the excited hole moves at its saturated drift velocity between the detector electrodes. This is a reasonable assumption for electrical frequencies presently of interest in that the time required for a hole to be accelerated from zero velocity to the saturated drift velocity is $5 \times 10^{-12}$ sec. for a bias of 1.0 volt across a $d = 10\mu m$ electrode separation. The corresponding length over which this acceleration occurs is $.2\mu m$. Thus, the assumption that the excited hole moves at its saturated drift velocity is valid for the traveling wave detector configuration being considered.

## 5. Signal Transmission Line Analysis

We now consider the effect of the incident radiation on the signal transmission line circuit. The equivalent transmission line of the traveling wave detector illustrated in Figure 2 is that of parallel strips with the optical waveguide between. The present analysis ignores the variation of light intensity normal to transmission line and thus considers the one-dimensional problem. The transmission line equations for instantaneous voltage $e(z,t)$ and instantaneous current $i(z,t)$ are:[22]

$$-\frac{\partial e(z,t)}{\partial z} = L_i \frac{\partial i(z,t)}{\partial t} \tag{27a}$$

$$-\frac{\partial i(z,t)}{\partial z} = G\, e(z,t) + C \frac{\partial e(z,t)}{\partial t} \tag{27b}$$

where $L_i$ is the transmission line series inductance per unit length, C is the shunt capacitance per unit length, and G is the shunt conductance per unit length. We have assumed the resistance of the conductors to be zero. The conductance G will vary according to the instantaneous light intensity due to the photoconductive effect. We continue our analysis by determining how G varies with z and t.

The induced conductivity $\sigma(z,t)$ is related to the hole concentration according to

$$\sigma(z,t) = e\,\mu_h\,p(z,t), \tag{28}$$

where $e = 1.6 \times 10^{-19}$ coulombs and $\mu_h$ is the hole mobility in Ge at the detector operating temperature (77°K). The value of $\mu_h$ at room temperature is $\mu_h \approx 2 \times 10^3$ cm$^2$/volt-sec.[2] If we assume the Au concentration in Ge is sufficiently small such that phonon scattering dominates scattering from ionized impurities, the value of $\mu_h$ approaches $1.54 \times 10^4$ cm$^2$/volt-sec. We assume that this value of $\mu_h$ is a reasonable estimate to the mobility of holes in Ge:Au at 77°K. The corresponding induced conductance $G(z,t)$ is given as[23]

$$G(z,t) = \sigma Z_e / Z_c \tag{29}$$

where $Z_c$ is the characteristic impedance of the two conductor transmission line of Figure 2 and $Z_e$ is the wave impedance of the thin-film medium at the frequency $\omega$:

$$Z_e \sim \frac{377}{\sqrt{\varepsilon_r}} \,. \tag{30}$$

For Ge $n_2 \cong \sqrt{\varepsilon_r}$ so that $Z_o \cong Z_e$. Finally, from the form of (15) using (28) and (29), we determine the result:

$$G(z,t) = G_o\, e^{-\alpha z} + (G_1\, e^{j(\omega t - hz)} + \text{c.c.})\, e^{-\alpha z} \,, \tag{31}$$

where:

$$G_o = (\alpha \xi_o / Z_c) E_L^{\,2} \tag{32a}$$

$$G_1 = 2(\alpha \xi_1 / Z_c) e^{-j\phi}\, E_L E_S. \tag{32b}$$

In (32), the phase angle $\phi$ is defined

$$\phi = \tan^{-1} \omega\tau, \tag{33}$$

and the constants $\xi_o$ and $\xi_1$ are defined as

$$\xi_o = \frac{e\mu_h \tau r}{h\nu_s} \tag{34a}$$

$$\xi_1 = \frac{e\mu_h \tau r}{2h\nu_s(1+\omega^2\tau^2)^{\frac{1}{2}}} . \tag{34b}$$

Now that we have determined the spatial and time variation of the conductance, we can examine solutions to the transmission line equations (27).

We determine the following differential equation for e(z,t) not involving i(z,t) from (27) in the usual manner.

$$\frac{\partial^2 e(z,t)}{\partial z^2} = L_i C \frac{\partial^2 e(z,t)}{\partial t^2} + L_i G(z,t) \frac{\partial e(z,t)}{\partial t} + L_i e(z,t) \frac{\partial G(z,t)}{\partial t} \tag{35}$$

We now solve (35) with G(z,t) specified by (31) by using the formalism developed for traveling wave parametric interactions. We consider a bias voltage applied to the transmission line of Figure 2 having amplitude $V_o$ and frequency $\omega_2$. With G(z,t) of the form (31) there will be an output voltage generated at frequency $\omega_1$, where

$$\omega_1 = \omega - \omega_2. \tag{36}$$

Both waves at $\omega_1$ and $\omega_2$ will have propagation constants $h_1$ and $h_2$ which, for TEM waves, are related to $\omega_1$ and $\omega_2$

$$h_1 = \omega_1/v_e \tag{37a}$$

$$h_2 = \omega_2/v_e \tag{37b}$$

We consider solutions to (35) for the instantaneous voltages $e_1(z,t)$ at $\omega_1$ and $e_2(z,t)$ at $\omega_2$ to be of the form:

$$e_1(z,t) = \tfrac{1}{2} V_1(z)\, e^{j(\omega_1 t - h_1 z)} + \text{c.c.} \tag{38a}$$

$$e_2(z,t) = \tfrac{1}{2} V_2(z)\, e^{j(\omega_2 t - h_2 z)} + \text{c.c.} \tag{38b}$$

We next substitute (38) into (35) and note that (35) will be satisfied at both frequencies $\omega_1$ and $\omega_2$. Now, if we make the usual parametric approximation of neglecting the second derivative since generally $V_1$ and $V_2$ vary sufficiently slowly, such that

$$\left| \frac{d^2 V_{1(2)}}{dz^2} \right| \ll \left| h_{1(2)} \frac{dV_{1(2)}}{dz} \right| , \tag{39}$$

we determine the following set of coupled mode equations.

$$\frac{dV_1(z)}{dz} = - Z_c G_0 e^{-\alpha z}\, V_2^*(z) - \tfrac{1}{2} Z_c G_1 V_1(z) e^{-\alpha z} e^{j\Delta h z} \tag{40a}$$

$$\frac{dV_2^*(z)}{dz} = - Z_c G_0 e^{-\alpha z} V_1(z) - \tfrac{1}{2} Z_c G_1^* V_2^*(z) e^{-\alpha z} e^{-j\Delta h z}. \tag{40b}$$

In (40), $G_0$ and $G_1$ are defined in (32) and

$$\Delta h = h - h_1 - h_2. \tag{41}$$

The quantity $\Delta h$ is a measure of the velocity mismatch in view of (37) and (13). Since $n \approx \sqrt{\epsilon_r}$ for Ge we will assume that $\Delta h = 0$ in what follows. Equations (40) are in the form of coupled mode equations which must be solved in order to specify the instantaneous voltages $e_1(z,t)$ and $e_2(z,t)$ in (38).

We can begin our solution of (40) by making the following independent variable transformation:

$$s = e^{-\alpha z} \tag{42a}$$

$$Z = -\frac{1}{\alpha} \ln s \tag{42b}$$

Incorporating this transformation into (40), the coupled mode equations now become:

$$\frac{dV_1}{ds} = \frac{Z_c G_o}{\alpha} V_1 + \frac{Z_c G_1}{2\alpha} V_2^* \tag{43a}$$

$$\frac{dV_2^*}{ds} = \frac{Z_c G_o}{\alpha} V_2^* + \frac{Z_c G_1^*}{2\alpha} V_1 \tag{43b}$$

which is the familiar form of the coupled mode equations. Equations (41) are solved by standard techniques[24] and taking those solutions and making the inverse substitution (42) gives:

$$V_1(z) = -V_o \exp\left[-Z_c G_o (1-e^{-\alpha z})/\alpha\right] \operatorname{Sinh}\left[Z_c |G_1| (1-e^{-\alpha z})/(2\alpha)\right] \tag{44a}$$

$$V_2^*(z) = \frac{(G_o - |G_1|/2)}{|G_1|} V_o \exp\left[-Z_c G_o (1-e^{-\alpha z})/\alpha\right]$$

$$\operatorname{Sinh}\left[Z_c |G_1| (1-e^{-\alpha z})/(2\alpha)\right] + V_o \exp\left[-Z_c (G_o - |G_1|/2)(1-e^{-\alpha z})/\alpha\right]. \tag{44b}$$

In determining the solutions (44) we assumed that the bias voltage $V_2(z)$ had amplitude $V_o$ at z=o and that the voltage $V_1(z)$ had zero amplitude at z=o.

We are interested in the values of $V_1(z)$ and $V_2(z)$ at the terminating load resistor of the transmission line, i.e., at z=L. At z=L, both solutions (44) involve terms $(1-e^{-\alpha L})$. As noted by Arams et al,[25] this factor is equal to the quantum efficiency $\eta$ of the detector if reflections are ignored. We indicated earlier that the advantage of the

traveling wave detection scheme was that the quantum efficiency limitation could be overcome by using a detector having a long length. To overcome this limitation then, our detector length L should be sufficiently long

$$L >> \alpha^{-1}$$

so that

$$\eta = (1-e^{-\alpha L}) \cong 1.$$

The voltage amplitudes $V_1(L)$ and $V_2^*(L)$ in (44) thus have the form

$$V_1(L) = - V_o \exp\left[-\xi_o E_L^2\right] \quad \text{Sinh} \quad \left[\xi_1 E_L E_S\right] \tag{45}$$

$$V_2^*(L) = (1+\omega^2\tau^2)^{\frac{1}{2}} \quad (E_L/E_S) V_o \exp\left[-\xi_o E_L^2\right] \quad \text{Sinh} \quad \left[\xi_1 E_L E_S\right]$$

$$+ V_o \exp\left[-\xi_o E_L^2\right] \quad \exp\left[\xi_1 E_L E_S\right] \quad , \tag{45b}$$

where (32) and (34) were used. In (45), we assumed $E_L >> E_S$.

Equations (45) can be further simplified if we consider the magnitude of $\xi_o$ and $\xi_1$ given in (34). To evaluate these quantities, we use the hole mobility of Ge $\mu_h$ = 1900 $cm^2$/volt-sec[18] , at 300°K and a hole lifetime $\tau = 10^{-10}$ sec., and anticipate that $\eta$ would have a value of around .8 in an optimally designed device. Using these values, we find

$$\xi_o = 1.3 \times 10^{-10} \ m^2/v^2$$

$$\xi_1 = 4.7 \times 10^{-11} \ m^2/v^2,$$

where $\omega/2\pi = 1.5 \times 10^9$ Hz was used. Typically, the local oscillator power incident on the detector is 1 mW. For this power

$$E_L = 4.34 \times 10^4 \ \text{"/m},$$

where we assumed the waveguide cross section was 2μ X 20μ. From these values it follows that

$$\xi_o E_L^2 = .24 \tag{46a}$$

$$\xi_1 E_L E_S << 1 \text{ for } E_s << E_L. \tag{46b}$$

We can thus approximate the Sinh functions in (45) by their arguments and the exp $[\xi_1 E_L E_S]$ term by 1 resulting in

$$V_1(L) = -V_o \exp[-\xi_o E_L^2] \xi_1 E_L E_S \tag{47a}$$

$$V_2(L) = V_o \exp[-\xi_o E_L^2] (1 + \xi_o E_L^2/2). \tag{47b}$$

Note that the output signal voltage $V_1(L)$ is proportional to the signal field amplitude $E_L$ as in a lumped circuit heterodyne detector and that the output bias voltage amplitude $V_2(L)$ is independent of the signal field. The equations (47) complete the transmission line analysis of the traveling wave detector.

## 6. Heterodyne Detector Performance Evaluation

We now determine the signal power and noise power delivered to the load in order to determine the signal-to-noise ratio and the minimum detectable power. These quantities will then be evaluated for the traveling wave Ge detector at $\lambda$ = 10.6 μ and compared to similar quantities for conventional heterodyne detectors at $\lambda$ 10.6 μ.

At this point we let the bias frequency $\omega_2 \to 0$ so that the signal frequency approaches the optical modulation frequency $\omega_1 \to \omega$. The signal voltage at z = L is given by (47). This voltage will encounter some reflection due to impedance mismatch. We assume that the fraction $\rho$ of the signal voltage appears across the load having resistance $R_L$. The current across the load due to the signal is thus

$$i_s = \rho V_1(L)/R_L$$

$$= -\rho V_o/R_L \exp[-\xi_o E_L^2] \xi_1 E_L E_S. \tag{48}$$

The mean square signal current is thus

$$\overline{i_s^2} = 2\rho^2 V_o^2/R_L^2 \exp\left[-2\xi_o E_L^2\right] \xi_1^2 E_L^2 E_S^2 \,. \qquad (49)$$

To obtain the signal-to-noise ratio, we must determine the corresponding quantity for the noise current.

One of the advantages of heterodyne detection is that one is able to control somewhat the noise properties of the detection system. By increasing the local oscillator power, the signal and the generation-recombination noise associated with the local oscillator power both increase at the same rate. Thus, the local oscillator power level is usually sufficiently high so that the generation-recombination noise associated with this power dominates other detector noise contributions. In calculating the signal-to-noise ratio, one only needs to include generation-recombination noise associated with the local oscillator power as other noise contributions can be made negligible in comparison.

The mean square current $\overline{i_n^2}$ in a frequency interval $\Delta\nu$ arising from generation-recombination noise associated with the local oscillator is given as[26]

$$\overline{i_n^2} = \frac{4e\bar{I}\,(\tau/\tau_d)\,\Delta\nu}{1+\omega^2\tau^2} \,, \qquad (50)$$

where $\bar{I}$ is the average current through the load resistor due to the local oscillator power and $\tau_d$ is the transit time of carriers between the electrodes. To determine $\bar{I}$, we must determine the voltage at z = L arising from the presence of the local oscillator power in the detector. With $E_s = 0$ and $E_L = 0$, $V_1(1)$ and

$$V_2(L)\Big|_{E_L = 0} = V_o \,. \qquad (51)$$

With $E_L \neq 0$ the voltage at z = L is given by (46). The voltage at z = L due to the presence of $E_L$ is thus that result minus (51). Assuming

that $\rho$ accounts for impedance mismatch as before, we find

$$\bar{I} \cong \rho \, V_o/R_L \exp [-\xi_o E_L^2] \, \xi_o E_L^2/2 \qquad (52)$$

for the average current passing through $R_L$.

The mean square noise current (50) will be fully specified once we determine $\tau_d$. We assume that the bias voltage $V_o$ applied to the transmission line is sufficiently high so that carriers generated all along the line travel between the two conductors with velocity equal to their saturated drift velocity. The transit time is thus constant for all carriers generated even though the voltage across the photoconductor varies along its length. If d is the width between the two transmission line conductors (i.e., w for slot and h for strip line) then $\tau_d$ is

$$\tau_d = d/v_d$$

$$= d^2/(\mu_h V_d) \quad , \qquad (53)$$

where $v_d$ is the saturated drift velocity and $V_d$ is the value of voltage which just saturates the drift velocity. For $\tau_d$ to be constant $V_o$ must be such that the minimum voltage along the transmission line $\approx V_d$. The minimum voltage along the transmission line is approximately $V_o \exp [-\xi_o E_L^2]$ so that

$$\tau_d = \frac{d^2}{\mu_h V_o \exp [-\xi_o E_L^2]} \quad . \qquad (54)$$

The mean square noise current (50) is now fully specified.

By substituting (54) and (51) into (50) we can determine the signal-to-noise ratio S/N. We find from (50) and (49) that $S/N = \bar{i}_s^2$ or

$$S/N = \rho r \left(\frac{d \, Z_o}{t \, Z_c}\right) \frac{P_s}{2 \, h \, \nu_s \, \Delta\nu} \quad . \qquad (55)$$

In (55) t is the waveguide thickness, we assumed that $R_L \approx Z_c$, and the signal power $P_s = A\, E_s^2/Z_o$.

The signal-to-noise ratio in (55) represents a factor times the quantum limit for heterodyne detection in a photoconductor, i.e.[27]

$$(S/N)_{\text{quantum limit}} = P_s/(2h\nu_s\Delta\nu). \tag{56}$$

We can thus define an efficiency $\eta_{eq}$ equivalent to the quantum efficiency in conventional heterodyne photoconductive detector as

$$\eta_{eq} = \rho r\, d\, Z_o/(t Z_c) \quad . \tag{57}$$

Equation (55) can now be written in a manner comparable to conventional heterodyne detection in photoconductors:

$$S/N = \eta_{eq}\, P_s/(2h\nu_s\Delta\nu) \quad . \tag{58}$$

The minimum detectable power $P_s^{min}$ is defined as that value which yields a signal-to-noise ratio of one. $P_s^{min}$ is given as

$$P_s^{min} = (2/\eta_{eq})\, h\, \nu_s\, \Delta\nu \quad . \tag{59}$$

For the traveling wave detector to have better performance than a conventional photoconductive detector, it is required that

$$\eta_{eq} > \eta \tag{60}$$

where $\eta$ is the quantum efficiency of the conventional detector.

The equivalent efficiency $\eta_{eq}$ involves factors relating to waveguide aspect ratio, transmission line impedance mismatch, and input signal coupling. The waveguide aspect ratio and input signal coupling are well defined features and can be calculated for a given configuration. However, the characteristic impedance and the impedance mismatch at the load resistor are problems which require further theoretical and experimental investigation.

## 7. Characteristic Impedance of a Traveling Wave Detector

In a traveling wave photoconductive detector optical radiation is detected because its presence changes the shunt conductance of an electrical transmission line. With an optical wave propagating in the photoconductive material colinearly and at the same velocity with an electrical wave along the electrical transmission line, the electrical wave experiences a cumulative change in shunt conductance. This cumulative change in shunt conductance continues until the optical wave has been completely absorbed. The analysis of the spatial and time dependence of the characteristic impedance of the electrical signal transmission line continues below.

The total conductivity of the Ge optical waveguide is composed of both a local oscillator portion $\sigma_L$ and a signal $\sigma_S$ where

$$\sigma = \sigma_L + \sigma_S \tag{61}$$

and

$$\sigma_L = \frac{e\mu_h \alpha\tau \; R}{4\hbar\omega_s} \; (S_L + S_S) \; e^{-\alpha z} \tag{62}$$

$$\sigma_s = \frac{e\mu_h \alpha\tau R \; e^{-\alpha z}}{2\hbar\omega_s (1 + \omega^2\tau^2)^{\frac{1}{2}}} \sqrt{S_L \; S_S} \left[ \text{Cos} \; (\omega t - hz - \phi) - \right. \tag{63}$$

$$\left. e^{-t/\tau} \; \text{Cos} \; (hz + \phi) \right] \quad ,$$

where (15), (23), and (28) were used. The peak local oscillator and signal power densities are $S_L$ and $S_S$. In determining $\sigma_L$ and $\sigma_S$ in (61) we assumed that the total transverse conductivity was one-half of the peak value, as this is the average value for $E_L$ and $E_S$ for the lowest order x-polarized mode.* Now that we have determined the conductivity of the material separating the two conductors of the transmission line as a function of z, we can determine the characteristic impedance of the transmission line as a function of z.

* This mode has lowest loss for the waveguide configuration of Fig. 2.

The problem of a two conductor transmission line in which the conductors are separated by a dielectric material having finite conductivity is treated by Collin.[23] The characteristic impedance of such a line is given as

$$Z_c = \frac{Z_{co}}{(1 - j\frac{\sigma}{\omega\varepsilon})^{\frac{1}{2}}} \quad , \tag{64}$$

where $Z_{co}$ is the characteristic impedance of the transmission line when the material separating the conductors has zero conductivity and $\varepsilon$ is the permittivity of Ge at the i-f ($140 \times 10^{-12}$ Farad/m). We neglect the conductivity of Ge when the signal and local oscillator fields are zero so $Z_{co}$ is the characteristic impedance of the transmission line of Figure 2 when no optical radiation is present.

We will evaluate $Z_c$ in (64) in terms of $Z_c/Z_{co}$, because we are mainly interested in the effect of the optical radiation on the characteristic impedance. Actual values of $Z_{co}$ for the structure of Figure 2 may be evaluated using a formal procedure,[16] or from Figure 7.

We consider first the presence of the local oscillator field only. Figure 9 is a plot of $|Z_c| / Z_{co}$ as a function of length for three different values of the parameter $\Omega$ where

$$\Omega = \frac{2\pi\tau S_L}{\omega} \quad . \tag{65}$$

Note that $\Omega$ allows for variations in local oscillator power density, the heterodyne frequency, and carrier lifetime. Figure 10 is a corresponding plot of the phase of $Z_c$ as a function of z. Note that $Z_c$ departs from $Z_{co}$ more as $\Omega$ increases or as $\tau$ or $S_L$ increases or as $\omega$ decreases. In all cases note that as z increases, $Z_c$ approaches $Z_{co}$. If the detector is 5 cm long, then the electrical i-f amplifier should be matched to the value of $Z_{co}$ at z = 5 cm in Figures 9 and 10. Table II lists some situations corresponding to the three curves of Figures 9 and 10. In Table II we consider variations of the basic design system in which $\tau = 10^{-8}$ seconds and $\omega = 2\pi\ (1.5 \times 10^9)$ rad/sec. It should be noted that for this

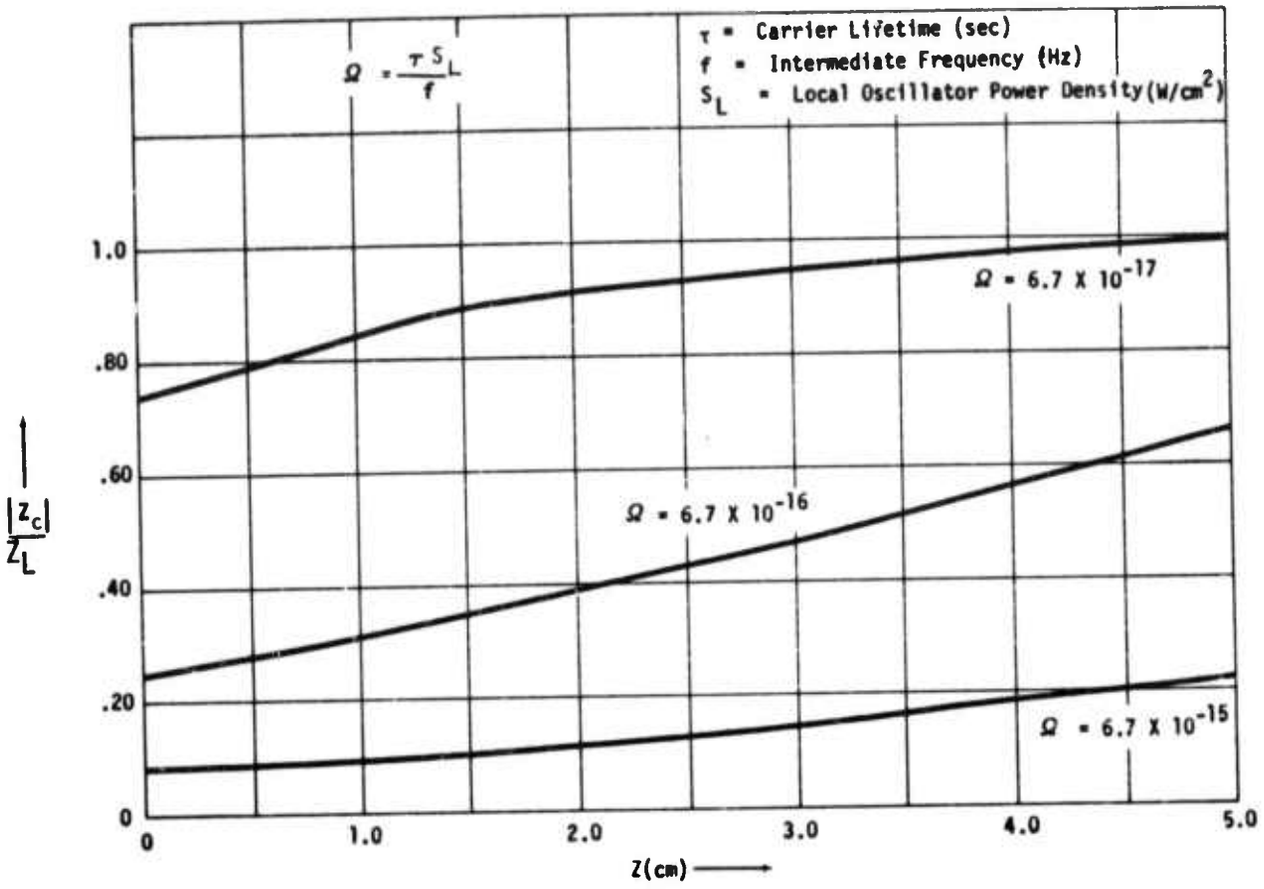


Figure 9. Traveling Wave Heterodyne Detector Characteristic Impedance as a Function of Length Carrier Lifetime and Local Oscillator Power Density

situation the high frequency roll-off term $(1 + \omega^2\tau^2)^{-\frac{1}{2}}$ in (64) = .01, implying that the detector response is reduced by this amount.

The results displayed in Figures 9 and 10 and Table II correspond to zero signal field. With a nonzero signal field these results are slightly altered. The conductivity in (64) now contains a factor $(1 + \sigma_S/\sigma_L)$ times the conductivity $\sigma_L$ used with no signal present. Since for heterodyne detection $S_S << S_L$ we find that

$$\frac{\sigma_S}{\sigma_L} = \frac{2}{(1 + \omega^2\tau^2)^{\frac{1}{2}}} \sqrt{\frac{S_S}{S_L}} \left[\text{Cos } (\omega t - hz - \phi) - e^{-t/\tau} \text{ Cos } (hz + \phi)\right] \quad (66)$$

Because this term is proportional to $S_S/S_L$, it is generally small. The effect of the signal field on the characteristic impedance is thus a small plane wave type modulation to the curves of Figures

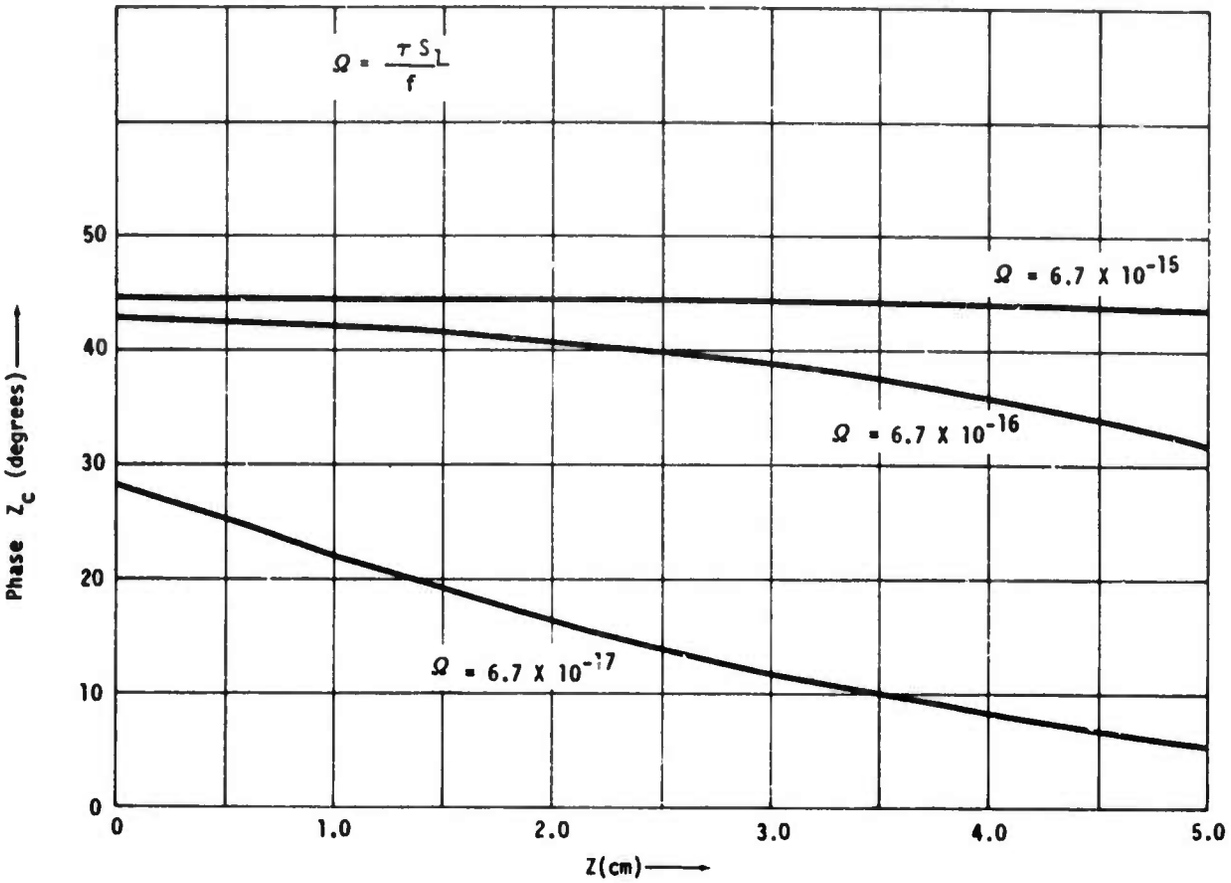


Figure 10. Traveling Wave Heterodyne Detector Characteristic Phase as a Function of Length Carrier Lifetime and Local Oscillator Power Density

9 and 10. The period of this spatial modulation is $2\pi/h = 5$ cm for $\omega = 2\pi\ (1.5 \times 10^9)$ rad/sec.

The question arises as to how this spatial variation of transmission line characteristic impedance affects waves propagating on this line. With a dc bias applied to the transmission line the presence of a signal optical field causes a time and spatial modulation of the shunt conductance. As a result an electrical signal wave at the heterodyne frequency is parametrically excited on the transmission line. Because electrical and optical velocities are matched, the effect is cumulative and the electrical signal increases as it propagates. If the characteristic impedance of the transmission line is rapidly changing over the span of an electrical wavelength, as it is for the curves in Figures 9 and 10, this electrical signal wave will not build up as fast as it would if the impedance were uniform.

TABLE II

Traveling Wave Heterodyne Detector Design Parameters

| | $S_L$ (W/cm$^2$) | $\omega/2\pi$ (Hz) | $\tau$ (sec.) |
|---|---|---|---|
| Case I | 1.0 | $1.5 \times 10^9$ | $10^{-7}$ |
| $\Omega = 6.7 \times 10^{-17}$ | 10 | $1.5 \times 10^9$ | $10^{-8}$ |
| | $10^2$ | $1.5 \times 10^{10}$ | $10^{-8}$ |
| Case II | $10^2$ | $1.5 \times 10^9$ | $10^{-8}$ |
| $\Omega = 6.7 \times 10^{-16}$ | | | |
| Case III | $10^2$ | $1.5 \times 10^8$ | $10^{-8}$ |
| $\Omega = 6.7 \times 10^{-15}$ | $10^3$ | $1.5 \times 10^9$ | $10^{-8}$ |
| | $10^4$ | $1.5 \times 10^9$ | $10^{-9}$ |

If the continuous impedance spatial variation reduces the electrical signal sufficiently, detection sensitivity will be reduced. In Section 5, the parametric build up of the electrical signal voltage $V_1$ (L) along the transmission line was determined. At the end of the detector section of transmission lines (z = L) we find $V_1$ (L) from equation (47) where $V_0$ is the bias voltage and $\xi_0$ and $\xi_1$ are constants given by (34a) and (34b).

In (47), the exponential term accounts for the cumulative impedance mismatch due to the local oscillator. Note that the higher the local oscillator power, the greater the degradation of the signal voltage in agreement with intuition. The exponential attenuation in (47) will be negligible ($\xi_0 E_L^2 << 1$) when the effect of the local oscillator on $Z_c$ is negligible ($\tau_L << \omega \varepsilon_0$). In the previous interim report, we examined the detector sensitivity by determining the signal-to-noise ratio and minimum detectable power for situations where the effect of the local oscillator on characteristic impedance was negligible. For the case in which the local oscillator significantly affects the characteristic impedance, the signal-to-noise ratio is degraded by the factor

$$e^{-\xi_0 E_L^2}$$

The minimum detectable power would thus be increased by a factor

$$e^{\xi_o E_L^2}.$$

Each of these factors become significant when

$$E_L^2 \sim 1/\xi_o$$

or when

$$S_L \approx \frac{1}{Z_o \xi_o} \simeq 10 W/cm^2 \quad , \tag{67}$$

where $Z_o$ is the optical impedance of the local oscillator waveguide mode.

## 8. Effect of Compensation on Carrier Lifetime

Because the carrier recombination lifetime limits the time response of the traveling wave detector, this recombination lifetime must be reduced in order to provide faster detector time response. Compensation by antimony provides one means to reduce the recombination lifetime. The Sb atoms enter the crystal as a shallow donor level. The Fermi level is correspondingly raised, thus increasing significantly the fraction of gold atoms having the excited state of interest occupied with an electron. Because the recombination rate is proportional to this fractional occupancy,[28,29] the excited hole lifetime is thus reduced. For conventional photoconductive detectors, the amount of compensation is limited because the increased fractional occupancy of the gold-excited state lowers the absorption coefficient. However, in a traveling wave detector, this limitation is not nearly so restrictive because this structure allows high device quantum efficiency even with materials having low absorption coefficients. Thus, compensation can be used to a much greater extent in crystals to be used in traveling wave detectors than those to be used in conventional photoconductive detectors.

Consider quantitatively the effect of compensation on gold-doped germanium. The hole recombination lifetime $\tau$ is given by the relation:[30]

$$\tau = \frac{1}{N_a^- \, v \, \sigma_h} \quad , \tag{68}$$

where $\sigma_h$ is the cross section for recombination, v is the hole thermal velocity, and $N_a^-$ is the concentration of ionized gold atoms. Throughout this analysis we consider only the gold acceptor level having energy $E_A$ = .15 ev above the valence band edge as this is the impurity level of interest for detector considerations. We let $N_a$ represent the total concentration of gold atoms in germanium.

As noted earlier, we wish to minimize $\tau$. From (68), we can do this by maximizing $N_a^-$. The absolute upper limit on the concentration of ionized impurities is the total impurity concentration $N_a$. Thus, the absolute lower limit of the hole lifetime is

$$\tau_{min} = \frac{1}{N_a \, v \, \sigma_h} \quad . \tag{69}$$

This limit can be reduced by increasing the concentration of gold atoms present in germanium. However, there is a limit of how great of an impurity concentration that can be introduced while maintaining a homogeneous solid solution.[31] This limiting concentration is referred to as the solid solubility limit. For gold in germanium, a reasonable value of this solubility limit is $2 \times 10^{16} cm^{-3}$.[32] At liquid nitrogen temperature, the recombination cross section[33] is $\sigma_h = 1 \times 10^{-13} cm^2$ and the average hole thermal velocity is v = $1 \times 10^{7}$ cm/sec.[30] Thus, the minimum recombination lifetime for Ge:Au is

$$\tau_{min} = 5 \times 10^{-11} \text{ seconds,}$$

as limited by the solid solubility of gold in germanium. However, as we shall see, approaching this value causes the absorption coefficient to approach zero, so a practical lower limit is somewhat larger.

Now, assuming we can add gold into germanium up to the solubility limit, we wish to consider how close the actual recombination lifetime $\tau$ can approach $\tau_{min}$. This, in turn, depends on how close the ionized impurity concentration $N_a^-$ approaches $N_a$. The ionized acceptor concentration is given by[18]

$$N_a^- = \frac{N_a}{1 + \frac{1}{4}\exp[(E_A - E_F)/K_B T]} , \tag{70}$$

where $E_A$ is the acceptor energy as measured from the valence band edge ($E_A$ = .15 ev for the gold level of interest in Ge), $E_F$ is the Fermi energy, $K_B$ is Boltzman's constant, and T is temperature. We note that the ionized impurity concentration depends on the Fermi energy and temperature. In what follows, we will be considering a fixed temperature of 77°K. Once we determine the Fermi energy, we can obtain $N_a^-$ from (70) and $\tau$ from (68). The Fermi energy may be obtained by solving the charge neutrality equation:

$$n + N_a^- = p + N_d^+ , \tag{71}$$

where n and p are the electron and hole concentrations, respectively; and $N_d^+$ is the ionized compensating donor concentration. For the nondegenerate semiconductor we are considering, n and p are given as

$$n = N_c \exp[-(E_g - E_F)/K_B T] \tag{72-a}$$

$$p = N_v \exp[-E_F/K_B T] , \tag{72-b}$$

where $E_g$ is the band gap and $N_c$ and $N_v$ are the conduction and valence band effective density of states defined according to:

$$N_c = 2\left(\frac{2\pi m^*_{de} K_B T}{h^2}\right)^{3/2} M_c \tag{73-a}$$

$$N_v = 2\left(\frac{2\pi m^*_{dh} K_B T}{h^2}\right)^{3/2} . \tag{73-b}$$

In (73) h is Planck's constant, $M_c$ is the number of equivalent minima in the conduction band ($M_c$ = 8 for Ge), and $m^*_{de}$ and $m^*_{dh}$ are the density of

state electron and hole effective masses. In (72) we have assumed that the zero along the energy axis corresponds to the valence band edge. The ionized donor concentration $N_d^+$ is related to the total compensating donor concentration by

$$N_d^+ = N_d \left\{ 1 - \frac{1}{1 + \frac{1}{2}\exp[(E_D - E_F)/K_B T]} \right\} , \qquad (73)$$

where $E_D$ is the donor energy as measured from the valence band edge. Now, substituting (74) and (72) into (71), the charge neutrality equation becomes

$$N_c \exp[-(E_g - E_F)/K_B T] + \frac{N_a}{1 + \frac{1}{4}\exp[(E_A - E_F)/K_B T]} =$$

$$N_v \exp[-E_F/K_B T] + N_d \left\{ 1 - \frac{1}{1 + \frac{1}{2}\exp[(E_D - E_F)/K_B T]} \right\} . \qquad (74)$$

Solution of this equation determines $E_F$, which then specifies $N_a^-$ from (69), which in turn specifies $\tau$ from (68). Because we are considering liquid nitrogen temperature, many approximations which allow simplification of (75) do not apply, and (75) must be solved numerically to determine $E_F$.

We consider first the case of no compensation; i.e. $N_d^+ = N_d = 0$. For this case, we use the tabulated semiconductor properties of Ge to obtain from (75) $E_F = .084$ ev. Assuming that we have the solid solubility limiting concentration of gold, the ionized acceptor concentration from (70) is

$$N_a^- = 2.76 \times 10^{12} \text{cm}^{-3} \quad \text{(no compensation)}$$

The corresponding recombination lifetime from (68) is thus

$$\tau = 3.62 \times 10^{-7} \text{sec.} \quad \text{(no compensation)}$$

We will now examine the effects of compensation.

Consider the addition of the compensation donor Sb ($E_D$ = .0096 ev) with concentration $N_d$. As $N_d$ increases, the Fermi energy $E_F$ as determined from (75) shifts upward. As $E_F$ increases, the ionized acceptor concentration (69) increases, causing a decrease in the recombination lifetime (68). This behavior is illustrated in Figure11, in which the hole recombination lifetime $\tau$ is plotted as a function of the compensating donor concentration $N_d$. Note that by controlling the amount of compensation added to Ge:Au, the lifetime can be varied between the maximum value which occurs for no compensation ($3.62 \times 10^{-7}$sec.) to the minimum value which occurs as the donor concentration becomes larger than the acceptor concentration ($\tau_{min} = 5 \times 10^{-11}$sec.).

We now consider the effect of compensation on the absorption coefficient. We are considering the absorption coefficient of Ge:Au at $\lambda$ = 10.6 $\mu$ to be due entirely to electron transitions from the valence band to the Au acceptor level. This is a reasonable assumption in that this is the only absorption process which contributes to the photoconductive response. The absorption coefficient in a semiconductor involving such a class of electron transitions can be written as

$$\alpha = \alpha_o \quad f_v \, (1 - f_a) \tag{75}$$

where $\alpha_o$ is the absorption coefficient when all valence band states are occupied and all acceptor states empty, $f_v$ is the fraction of valence band states involved in the valence band-acceptor transition excited by $\lambda$ = 10.6 $\mu$ photons which are occupied, and $f_a$ is the fraction of acceptor states occupied (ionized). At the temperature of interest, $f_v$ is given as

$$f_v \cong 1 \tag{76}$$

independent of compensation doping, while $f_a$ is given as

$$f_a = \frac{N_a^-}{N_a} \quad , \tag{77}$$

which is a strong function of compensation donor concentration. Substituting (77) and (76) into (75) and taking $\alpha_o$ = .4 $cm^{-1}$, the absorption coefficient can be written as

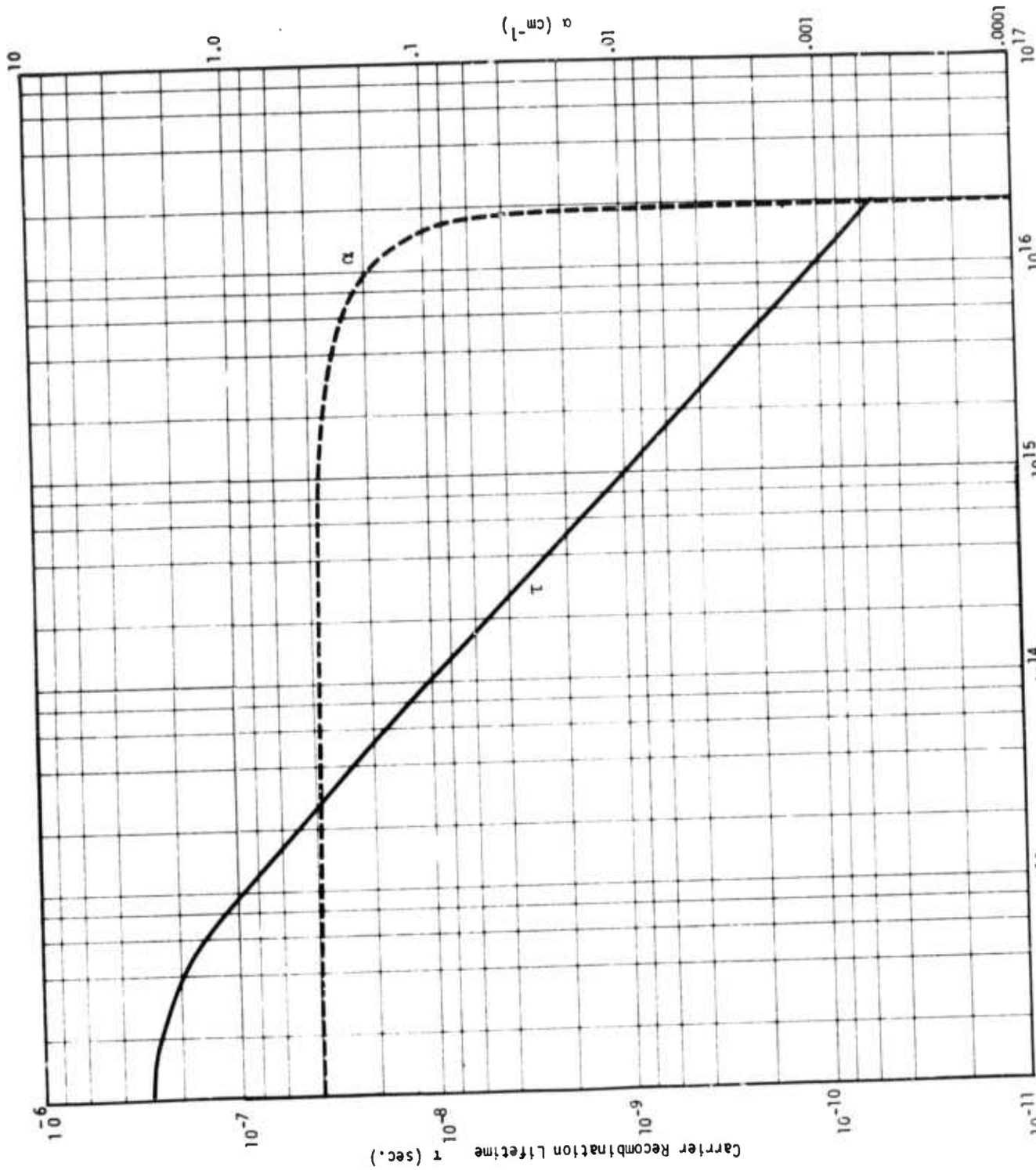


Figure 11. Effect of Sb Compensation Upon Carrier Recombustion Lifetime and Net Absorption

$$\alpha = .4 \left(1 - \frac{N_a^-}{N_a}\right). \qquad (78)$$

Now, as the compensation doping increases from zero, the Fermi level as given by the solution of (75) shifts upward. This increase in $E_F$ causes a significant increase in $N_a^-$ from (70) as the compensation donor concentration increases. In view of (78), the absorption coefficient will thus decrease as the compensation donor concentration increases and approach zero as $N_a^- \to N_a$. This behavior is illustrated in the plot of $\alpha$ versus $N_d$ in Figure 11 for the parameters used previously in the calculation of $\tau$ as a function of $N_d$ (also shown in Figure 11). We note that $\alpha$ remains nearly constant until $N_d \to N_a$. For example, if a lifetime of $10^{-10}$ sec. is desired, a donor concentration of $10^{16}$cm.$^3$ is required. For this degree of compensation the absorption coefficient has been reduced from $\alpha = .4$ cm.$^{-1}$ (no compensation) to $\alpha = .2$ cm.$^{-1}$ As any further decrease of $\tau$ causes a significant decrease in $\alpha$ (as shown in Figure 11), $\tau = 10^{-10}$ sec. can be considered a practical lower limit for recombination lifetime.

9. Optical Waveguide Attenuation Due to Metal Side Walls

The attenuation in the Ge optical waveguide due to the presence of gold electrodes has been determined as a function of electrode separation w or h, as shown in Figure 2 and 7. As noted previously, this electrode absorption must be minimized as optical energy absorbed in the metal electrodes reduces the detector quantum efficiency.

Our approach in considering the metal wall loss in the structure of Figure 7 is to consider a slab waveguide to exist in the y direction as well as in the x direction. We approximate the rectangular waveguide of Figure 2 by two orthogonal slab waveguides. Marcuse[34] indicates that this procedure yields an accurate determination of the waveguide mode propagation parameters as long as the mode in question is not close to being cutoff. We anticipate that the modes of interest in the traveling wave detector structure of Figure 2 will be far from the cutoff condition.

Thus, considering the metal walls to form a slab waveguide in the y direction, the mode attenuation constant can be determined by solving the slab waveguide eigenvalue equation. Solution of this equation for

metal wall structures is more difficult than for dielectric structures because of the complex dielectric properties of metals. Numerical solutions of the metal wall slab waveguide problem have been published by Takano and Hamasaki[35], Reisinger[36] and Kaminow, Mammel and Weber.[37] In addition, Batchman and Rashleigh have considered related aspects of this problem,[38] while Garmier and Stoll treat a related problem.[39] Although calculations presented in these papers are for visible wavelengths, the results indicate that the lowest loss waveguide mode would be the lowest order mode having the electric field tangential to the metal boundary.

The loss coefficient $\alpha_e$ of Ge and GaAs dielectric waveguide with two metallic walls (Au bias electrodes as depicted by the inserts of Figure 7) has been plotted in Figure 12 for the lowest order modes of both polarizations at $\lambda$ = 10.6 μm as a function of the electrode separation w or h. Note that the notation $TE_0$ implies that the electric field is tangential to the metal boundary. The curve of Figure 5 depicting loss for the $TE_0$ mode as determined by the asymptotic approximation[37] agrees quite well with the curve presented in a previous interim report determined by the perturbation approach.[3]

The loss curves for the $TM_0$ modes in Figure 12 (TM refers to modes having electric field perpendicular to the metal boundaries) are independent of electrode separation w in contrast to the $TE_0$ modes in which $\alpha_e$ drops off with increasing w. This contrasting and anomalous behavior occurs for the two lowest order TM modes because in the high frequency limit these two modes become the symmetrical and antisymmetrical surface plasmon modes.[36] The field for these modes is concentrated near the metal boundary.

In the case of TE modes in Figure 12 for two different dielectric waveguides, we note that the one with higher dielectric constant (Ge) has the lowest loss. This result is due to the higher field confinement in the Ge waveguide for TE modes. For the TM modes, the reverse is seen in Figures 5, i.e., the loss for the higher dielectric constant (Ge) structure is greater. This is due to the fact that for TM modes the electric field is concentrated at the metal boundary and that this concentration is greater for the higher dielectric constant waveguide material.

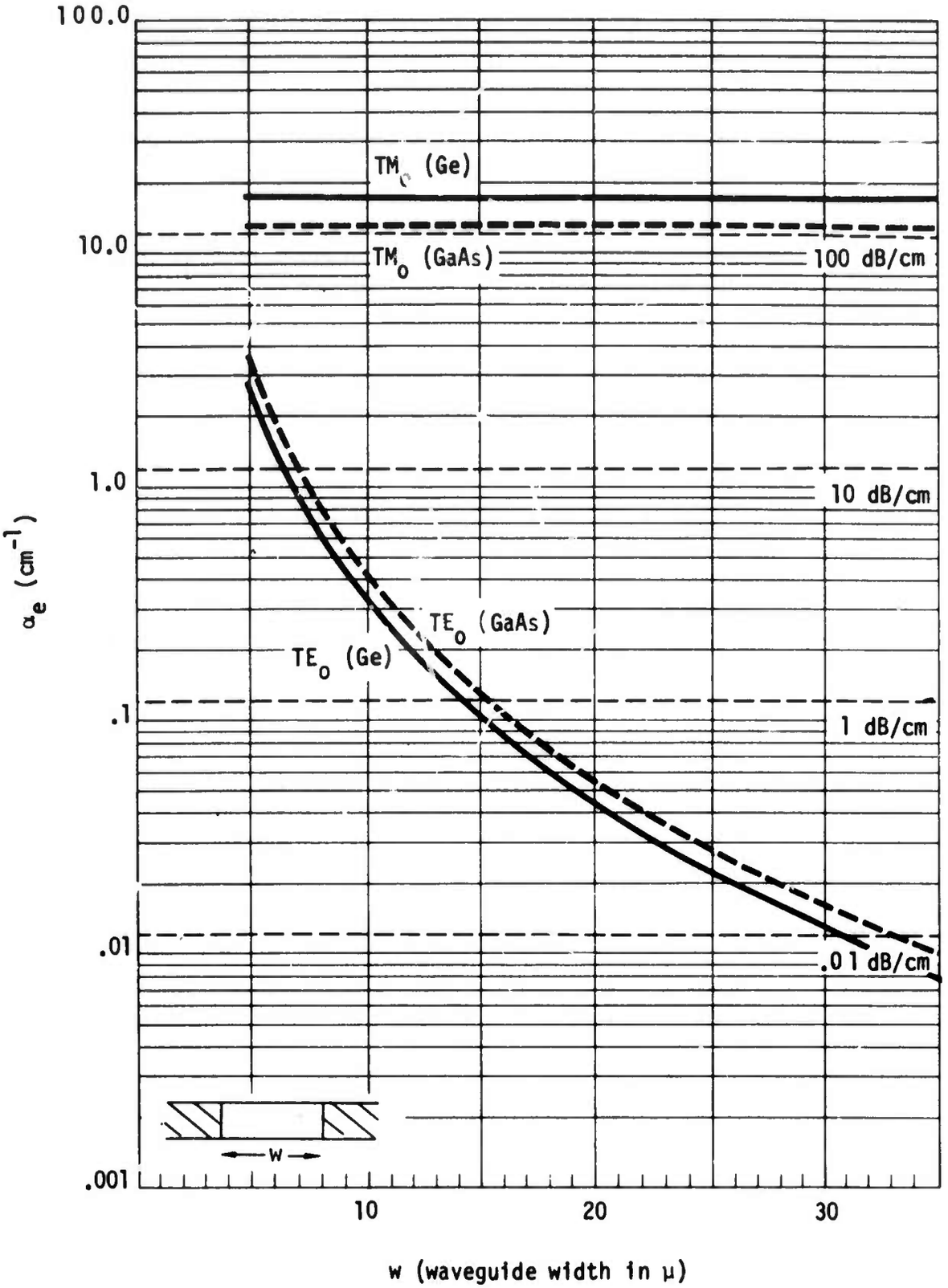


Figure 12. Absorption of Thin-Film Waveguide Due to Presence of Metallic Wall as Illustrated in Cross Section

The traveling wave detector structure is designed so as to utilize the lowest loss mode, the $TE_o$ mode. Note that the attenuation for $w < 10\mu m$ is quite severe. The results in Figure 12 were determined for room temperature values of the dielectric properties of gold, whereas the loss at 77° is actually slightly less. In order that the absorption due to metal walls does not seriously degrade detector quantum efficiency, $\alpha_e$ should be much less than the Ge absorption coefficient, i.e.,

$$\alpha_e << .4 \text{ cm}^{-1} \quad .$$

This condition implies that $w = 20\mu m$ is the minimum electrode separation which would provide a sufficiently low loss for satisfactory traveling wave detector operation.

10. Traveling Wave Heterodyne Detector Receiver Sensitivity

In addition to the ultrawide bandwidth due to the phase matching of the infrared signal and the down-converted output signal in the collinear waveguides of the heterodyne detector, two other additional advantages accrue. First, the small waveguide cross section reduces the required local oscillator power, even though the electric field in the guide is high (approaching breakdown). Second, and of the utmost importance, is the reduction of transit time across the waveguide width. Its effect is shown by computing the conversion gain and, thus, receiver system sensitivity.

The heterodyne detection receiver sensitivity is given by[40-43]

$$NEP = \frac{2h\nu_s\bar{\Delta f}}{\eta} + \frac{k(T_d + T_{if})\bar{\Delta f}}{G} \qquad (79)$$

where NEP = Noise Equivalent Power (S/N = 1, Watts)

$\bar{\Delta f}$ = IF Bandwidth

$T_d$, $T_{if}$ = Detector and IF input noise temperature

h, k = Planck's and Boltzmann's constants

where G = available conversion gain
defined as

$$G = \frac{\eta\, qV}{2h\nu_s} \left(\frac{\tau}{T_r}\right) \frac{1}{1 + \omega^2\tau^2} \qquad (80)$$

where $\eta$ = quantum efficiency
$q$ = electronic charge
$V$ = photoconductor bias
$\nu_s, \omega$ = optical signal and IF angular frequencies
$\tau$ = majority carrier lifetime
and $T_r$ = carrier transit time.

The first term of Eq. (79) represents the fundamental quantum noise limit of infrared detection increased by the factor $2/\eta$. The factor 2 arises from generation-recombination noise in photoconductivity. Unit quantum efficiency requires total absorption and conversion as free carriers without reflection or scattering.

The second term of Eq. (79) represents the detector Johnson noise and IF amplifier noise. Its suppression requires high conversion efficiency, thus, gain high quantum efficiency is required ($\alpha\ell \approx 2$ long absorption length). Also, a short carrier lifetime is required (achieved compensation) for wide bandwidth.

The available conversion gain given by Equation (80) is depicted in Figure 13 for three values of the majority carrier lifetime ($\tau = 10^{-8}$, $10^{-9}$, $10^{-10}$ sec) as a function of the base bandwidth. Two conversion gain scales are provided for two values of the carrier transit time ($T_r = 10^{-8}$, $10^{-9}$ sec). Figure 13 dramatically illustrates the requirement to achieve a reduced carrier lifetime through compensation in order to obtain large base bandwidth.

For the traveling wave detector configuration, an important design parameter, IF resistance $R_o$ with a local oscillator power $P_{LO}$ (watts)

$$R_o = \frac{w^2}{q\mu N} \frac{1}{(1 - e^{-\alpha\ell})} \qquad (81)$$

where w is the inter-electrode separation and the waveguide width, $\ell$ is the length of the infrared waveguide, $\alpha$ is the intensity absorption

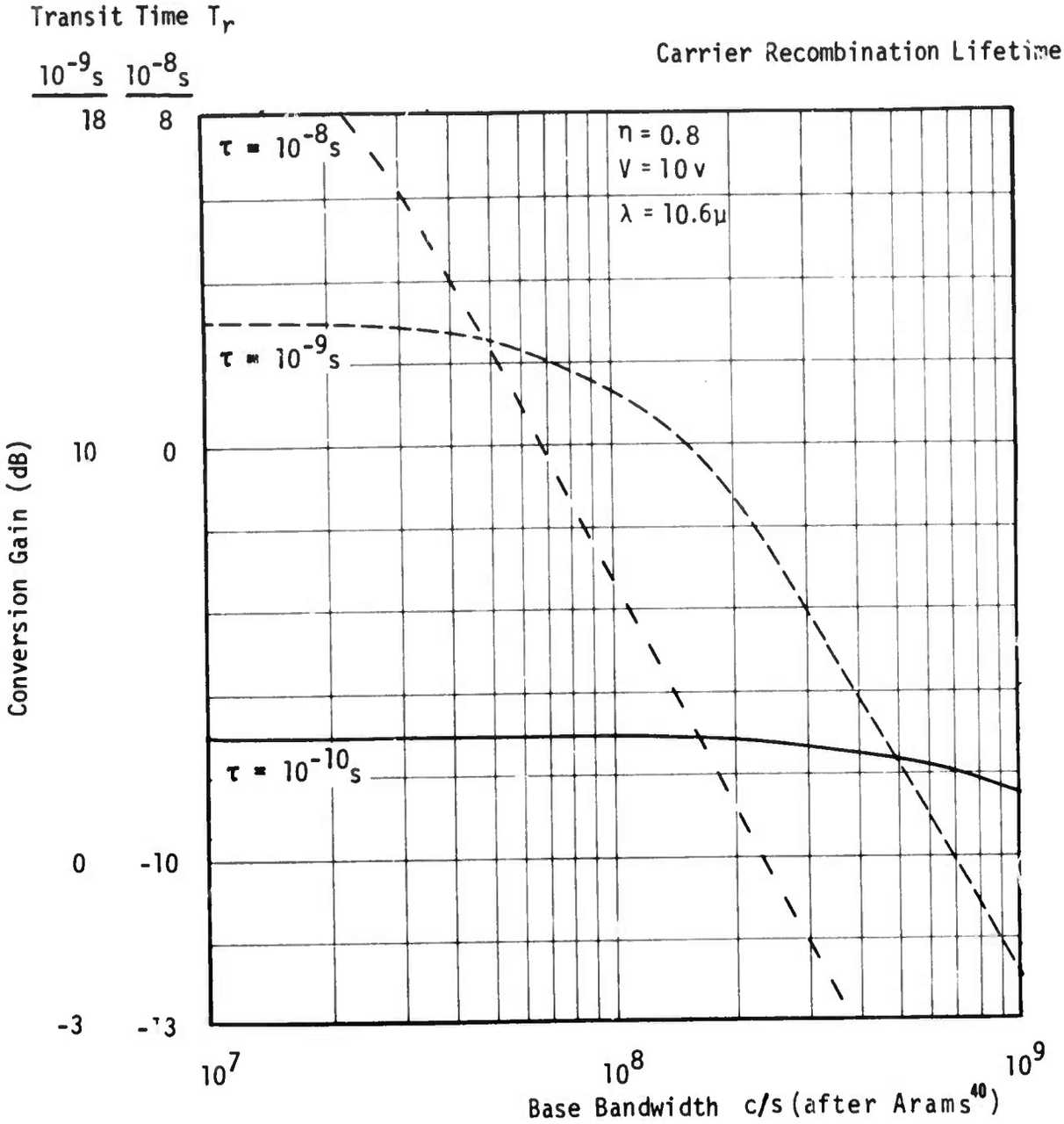


Figure 13. Conversion Gain of Heterodyne Photoconductive Detector as a Function of Frequency for Various Material Time Constants

coefficient, q = 1.6 X $10^{-19}$ coulombs is the electronic charge, and μ (= 1900 $cm^2$/volt-sec. for holes in germanium) is the free carrier mobility. N is the total number of free carriers generated in the sample, given by

$$N = \tau \eta P_{lo}/h\nu_{lo} \qquad (82)$$

where $\tau$ is the free carrier lifetime (about $10^{-8}$ sec. for holes in Ge:Au, $\eta$ is the quantum efficiency for absorption (assume $\eta = 0.5$), $h = 6.6256 \times 10^{-27}$ erg-sec is Planck's constant, and $\nu_{lo} = 3 \times 10^{13}$ $sec^{-1}$ is the local oscillator frequency and power of 20 microwatts, the number of free carriers generated is $N = 0.5 \times 10^{7}$. The IF resistance for a waveguide of 3 microns width is then 60 ohms. The total photoconductive detector capacitance $C = \epsilon \ell d/w$ (without considering the traveling wave nature) having length $\ell = 5$ cm, height $d = 2$ microns, and width $w = 3$ microns is $1.8 \times 10^{-12}$ farad, giving an $R_o C$ time constant of $10^{-10}$ sec for the detector.

In the microwave spectrum, it is customary to compare the performance of receivers by defining a noise factor. In the infrared, where the fundamental limit is quantum noise, the quantum-noise factor for a photoconductive heterodyne receiver is given by

$$QF = \frac{2}{\eta} + \frac{K(T_d + T_{if})}{h\nu_s G} \qquad (83)$$

For the ideal coherent heterodyne receiver, QF = 1 (0 dB) and is independent of $\Delta f$. The 0 dB reference level at 10.6 microns corresponds to a NEP = $1.87 \times 10^{-20}$ W/Hz. Typical experimental infrared heterodyne receivers approach this reference level within 6 - 20 dB.[41]

The expected performance of the traveling wave heterodyne detector is tabulated in Table III where the effects of carrier lifetime are to be noted. The advantage of short transit time because of the narrow waveguide width and large bias field, contribute significantly to the available conversion gain. When the conversion gain is large, the dominant contribution to NEP becomes the quantum efficiency and in turn, the absorption length, which appears as the dashed line for Ge:Au) in Figure 1. Calculated generation-recombination noise is on the order of $10^{-9}$ W, and the shot noise is $10^{-8}$ W. Therefore, a local oscillator of $10^{-5}$ W masks these contributions only when the available conversion gain is large.

The first example cited in Table III considers a transit time of $2 \times 10^{-11}$ seconds, due to the three-micron electrode separation and also considers uncompensated Ge(Au) with a typical hole lifetime of $10^{-8}$

TABLE III

TRAVELING WAVE PHOTOCONDUCTIVE HETERODYNE DETECTOR DESIGN PARAMETERS

| | | | |
|---|---|---|---|
| Waveguide Cross Section | 2 x 3 μm | 2 x 30 μm | 500 x 1000 μm |
| Bias Voltage | $2.3 \times 10^{-1}$ | 2.3 V | 38 Volts |
| Bias Electric Field | 770 | 770 | 770 Volt/cm. |
| Local Oscillator Power | 20 μW | 200 μW | 1.6 W |
| Local Oscillator Power Density | 330 | 330 | 330 Watts/$cm^2$ |
| $(1-e^{-\alpha\ell})$ Absorption Efficiency $\alpha = 0.4\ cm^{-1}$, $\ell = 5.7$ cm | 0.9 | 0.9 | 0.9 |
| Hole Lifetime $\tau$ | $2 \times 10^{-9}$ | $2 \times 10^{-9}$ | $2 \times 10^{-9}$ |
| Transit Time $T_r$ | $2 \times 10^{-11}$ | $2 \times 10^{-10}$ | $4.2 \times 10^{-9}$ |
| Number of Free Carriers Generated | $1.6 \times 10^{6}$ | $1.9 \times 10^{7}$ | $1.6 \times 10^{11}$ |
| Maximum Available Conversion Gain: | | | |
| $(IF << 1/\tau)$ | | 19.2 dB | |
| $(IF = 1\ GHz)$ | | -2.8 dB | |
| $T_d$ | | 77°K | |
| $T_{IF}$ | | 600°K | |
| Noise Equivalent Power/Bandwidth: | | | |
| $(IF << 1/\tau)$ | | $4.4 \times 10^{-20}$ Joules | |
| $(IF = 1\ GHz)$ | | $6.2 \times 10^{-20}$ Joules | |
| Quantum Noise Factor = $\frac{NEP}{h\nu_s B}$ : | | | |
| $(\omega_{IF} << 1/\tau)$ | | 3.5 dB | |
| $(IF = 1\ GHz)$ | | 4.9 dB | |

seconds. The minimum bias required to give this transit time is 230 millivolts. The electric field of 770 volts/cm applied to the photoconductive waveguide walls is near the limit of 800 volts/cm, beyond which the carrier mobility would decrease. Table III listing parameters for three waveguide cross sections has been designed to employ the same bias potential gradient and local oscillator power density which leads to three different values of the transit time, all of which leads to the same maximum available conversion gain. A detector temperature of 77°K and an IF amplifier effective noise temperature of 600°K has been assumed to compute the NEP and QF which are the same for each of these waveguide cross sections.

Table IV indicates the calculated performance showing the effect of reduction of carrier lifetime by compensation and increase of carrier transit time by reduced bias. The first column of Table IV is a repeat of the center column of Table III. However, two values of the IF amplifier noise figure are employed; namely, 3 dB and 8.5 dB, the latter corresponding to the experiments. The half power bandwidth based upon the change of available conversion gain is also included. The effect of Sb compensation reducing the carrier lifetime produces a dramatic increase of the calculated bandwidth. The effect of reduced bias increasing the carrier transit time has a dramatic effect upon the conversion gain, however, with a lesser effect upon the quantum noise factor. Table IV also indicates the effect of the IF amplifier noise figure upon the heterodyne receiver quantum noise factor. Degradation of the detector absorption efficiency leads directly to a deterioration of the quantum noise factor and the additional effect from the IF amplifier.

TABLE IV

TRAVELING WAVE PHOTOCONDUCTIVE HETERODYNE DETECTOR DESIGN PARAMETERS

| | | | |
|---|---|---|---|
| Waveguide Cross Section | 2 x 30 μm | | |
| Bias Voltage | 2.3 Volts | | |
| Bias Electric Field | 770 V/cm | | |
| Local Oscillator Power | 200 μW | | |
| Absorption Efficiency | 0.9 | | |
| Hole Lifetime $\tau$ | $2 \times 10^{-9}$ | $10^{-10}$ | $10^{-10}$ sec. |
| Transit Time $T_r$ | $2 \times 10^{-10}$ | $2 \times 10^{-10}$ | $2 \times 10^{-9}$ sec. |
| Available Conversion Gain: | | | |
| (IF < $1/\tau$) | 19.2 dB | 6.19 dB | -3.8 dB |
| (IF = 1 GHz) | -2.8 dB | 4.75 dB | -5.25 dB |
| $T_d$ | 77°K | 77°K | 77°K |
| $T_{IF}$ | 600°K 2123°K | 600°K 2123°K | 600°K 2123°K |
| Quantum Noise Factor = $\frac{NEP}{h\nu_s B}$ : | | | |
| (IF << $1/\tau$) | 3.5 dB 3.5 dB | 3.7 dB 4.1 dB | 5.2 dB 7.7 dB |
| (IF = 1 GHz) | 4.7 dB 7.1 dB | 3.8 dB 4.4 dB | 5.8 dB 8.6 dB |
| Bandwidth $\Delta f_{3\ dB}$ | 80 MHz | 1.6 GHz | 1.6 GHz |

## II. Coupling Considerations

It is essential that efficient coupling techniques be employed for the input signal to the traveling-wave heterodyne detector because of the direct effect upon the receiver sensitivity. It is also necessary to couple the local oscillator, however, not necessarily efficiently. Both the signal and local oscillator fields must be aligned sufficiently such that their spatial interaction yields a constructive phase front. This problem of coupling and alignment of the signal and local oscillator beams to conventional photoconductive and photovoltaic detectors has been adequately treated in the literature for a variety of transverse field distributions.[44-45] This aspect will not be duplicated herein except to draw parallels and distinctions with waveguides. In the case of beam/waveguide coupling, the coaxial alignment must be sufficient such that the spatical fields yield constructive phase fronts within the waveguide which thus requires identical mode spatial orders for an efficient response.

Communication and sensor systems employ propagating beams in free space which are collected by an aperture usually a refractive or reflective telescope system. The essential elements of this coupling are illustrated in Figure 14, composed of a refractive lens and an immersion lens (Weirstrass sphere), together with the input waveguide and its substrate.

Beam/waveguide couplers are in common use in integrated optics. They are the prism, grating, end-fire (taper) and diffraction with or without an immersion lens. The operation of the prism and grating coupler is both frequency and angle sensitive, which translates into changes of the waveguide mode order. The end-fire coupler through the substrate and the immersion lens are usually employed for the lowest order waveguide mode. Displacement and beam alignment with the taper coupler and immersion lens translate into loss of coupling efficiency through diffraction. The immersion lens exhibits the least spectral sensitivity other than that due to the material and antireflection coating.

The immersion lens is employed with a convergent beam to reduce the physical dimensions of the transverse field distribution within the dielectric so as to match the field distributions of waveguides restricted to the lower order modes. Its necessity is emphasized when the effective waveguide refractive index is large as in the case of Ge waveguides on GaAs substrates.

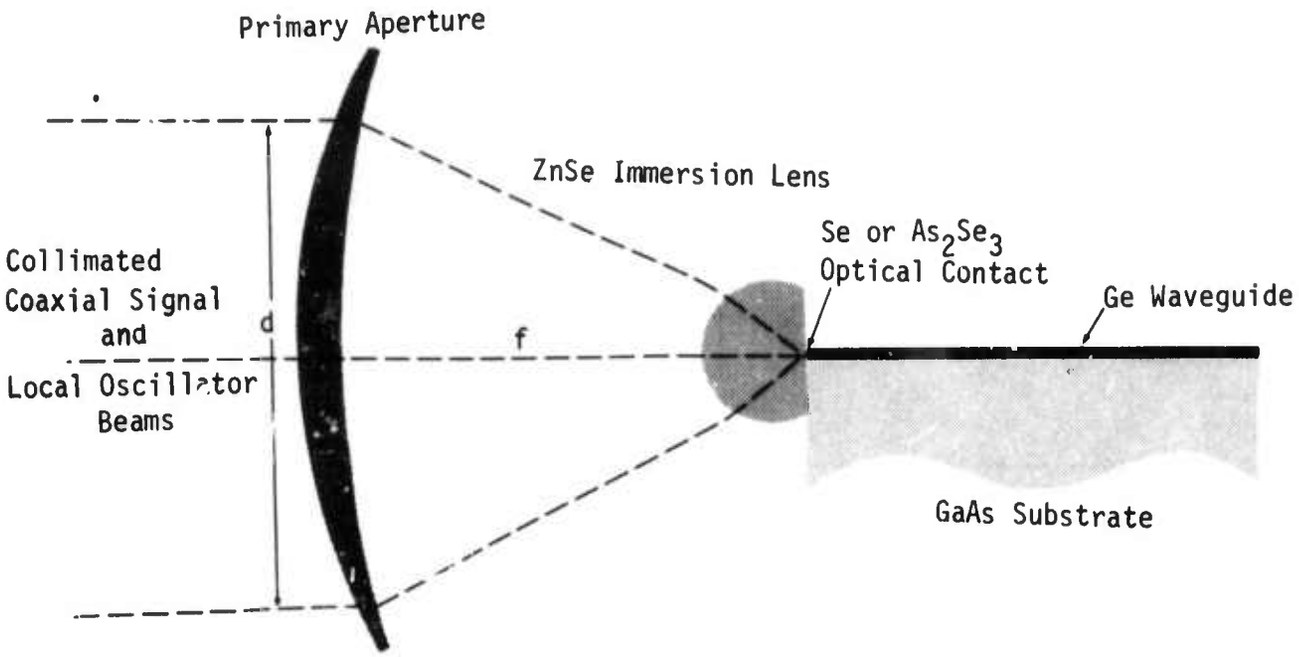


Figure 14. Beam/Waveguide Coupling

The immersion lens is employed in the form of a cylinder to match the rectangular waveguide cross sectional dimensions which usually approximate the wavelength in only one axis. One practical requirement must be fulfilled; that is achieving an optical contact between the lens and the waveguide. Failure to achieve this requirement in high-index materials leads to total internal reflection rather than coupling between the elements. The use of amorphous Se and $As_2Se_3$ or $As_2S_3$ partially fulfills this requirement. These materials have relatively low melting points and may be applied to the III-V and II-VI semiconductors after proper surface treatment, followed by pressing the interfaces together. The immersion lens in the form of the cylinder has been employed entirely throughout this effort where efficiency is required and where the waveguide transverse cross sectional dimensions are on the order of a wavelength. The use of a high refractive index immersion lens obviously requires an antireflection coating on the circular face. Simple diffraction coupling (without immersion lens) is usually employed as an expedient solution where the coupling efficiency is unimportant when determining other parameters such as the base band frequency response.

The design of an infrared telescope coupling to a single-mode optical waveguide has its roots in coherent high-power microscopy[49] and in the microwave

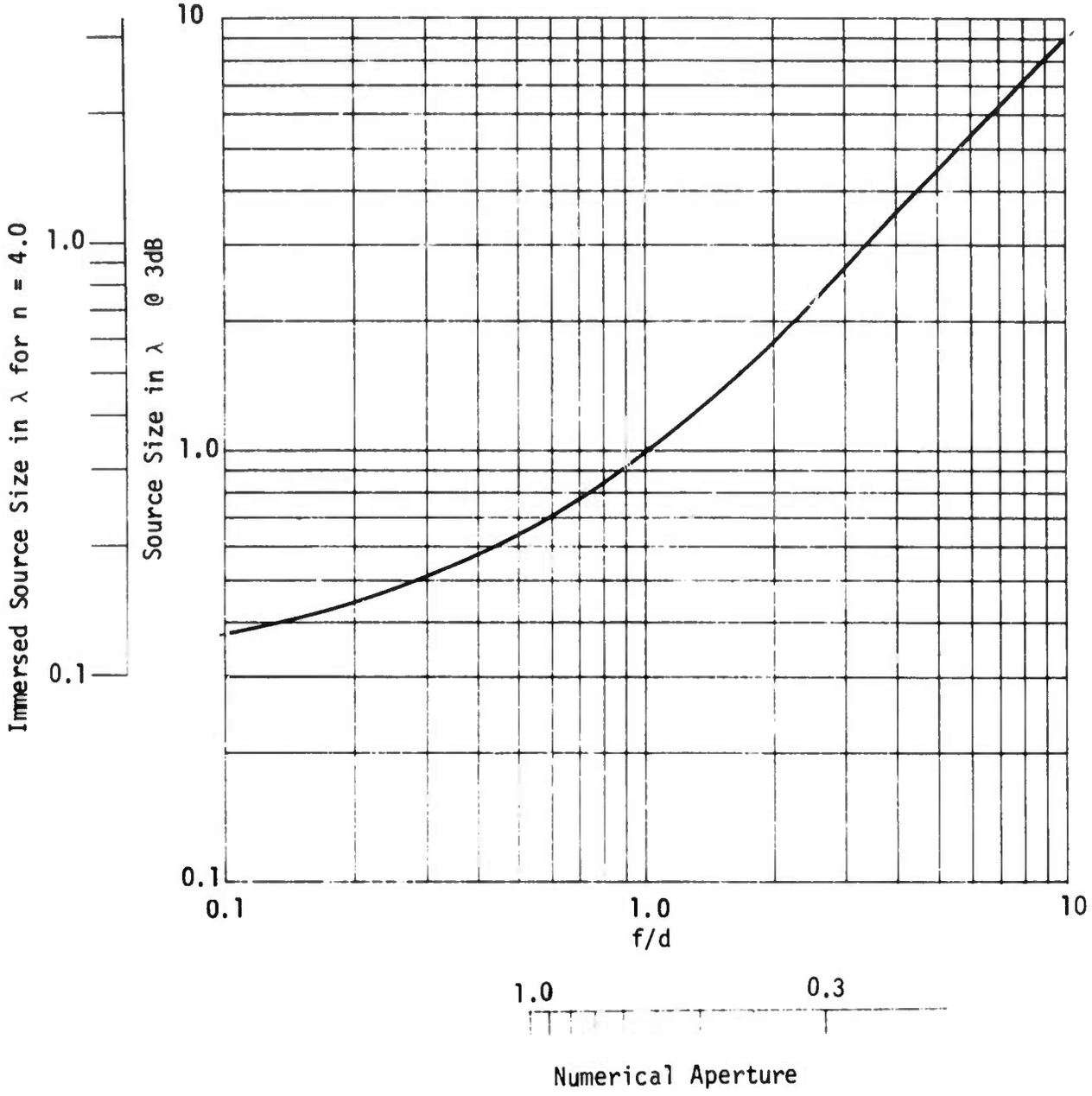


Figure 15. Focus Source Size as Function of Lens Numerical Aperture

antenna art.[48] The source size; that is, the width of the waveguide distribution for a focused aperture for a function of f/d, is depicted in Figure 15 where the source size is measured in wavelengths at the 3 dB contour where n = 1. An additional scale has been included for the source immersed in a dielectric such as Ge where n = 4. The corresponding numerical aperture scale is also included. Conventional infrared telescopes have an f/d = 3 more or less; whereas microscope objectives and microwave parabolic antennas tend toward f/d < 1. Large astronomical telescopes tend toward f/d ~ 10.

The collecting aperture and focusing function may encompass additional elements which change the f/d ratio. For a long focal length telescope f/d > 1, directivity is required in the waveguide source which is obtained by employing an image plane displaced from the center of the immersion lens, thus providing positive power. For a short focal length telescope f/d < 1, the image plane is positioned at the center, preferably with an immersion lens refractive index greater than that of the waveguide.

Telescope[49] or antenna design[48,50] for spatially coherent signals usually centers around an optimum--the efficient use of available aperture by maximization of the product of several factors. The first term is the fraction of the total power at the focus that is intercepted by the collecting aperture and thus is available as a plane wavefront to form the radiated directive diffraction pattern. The reciprocal function also holds, becoming the fraction of the incident power absorbed at the focus. This factor increases as the collecting aperture angular size $\psi$ increases until all energy radiated by the source (absorbed by the detector) is intercepted. The second factor is the efficiency with which the collecting aperture concentrates the available power into a single direction to form the principal lobe. The second factor is determined by the amplitude and phase distribution across the aperture and is a maximum when both are uniform. The presence of aberrations and apodisation decreases. It also decreases as the angular size of the collecting aperture increases because the illumination over the aperture tapers from a maximum value at the center to a lesser value at the edge--apodisation. The taper elimination results in a reduction of the near side lobes and increases the principal diffraction lobe beamwidth with a corresponding reduction of the directivity maximum. This taper is caused by both the directivity of the primary source at the focus and the space attenuation due to spherical geometry.

The effect of these factors upon the performance of a detector assuming uniform Gaussian and Airy distributions has been considered, including the aperture blocking of a Cassegrainian collecting system. The effect of these factors $G_f(\psi)$ assuming cosinusoidal distributions is shown in Figure 16. This figure shows that the directivity is a maximum when the angular source size encompasses all of the radiation from an isotropic source (n=0). Further, the gain factor is reduced as the primary source directivity is increased

$$G_f(\Psi) = 2(n + 1)\cos^n\Psi, \qquad 0 \leq \Psi \leq \frac{\pi}{2}$$

$$= 0, \quad \Psi > \frac{\pi}{2} .$$

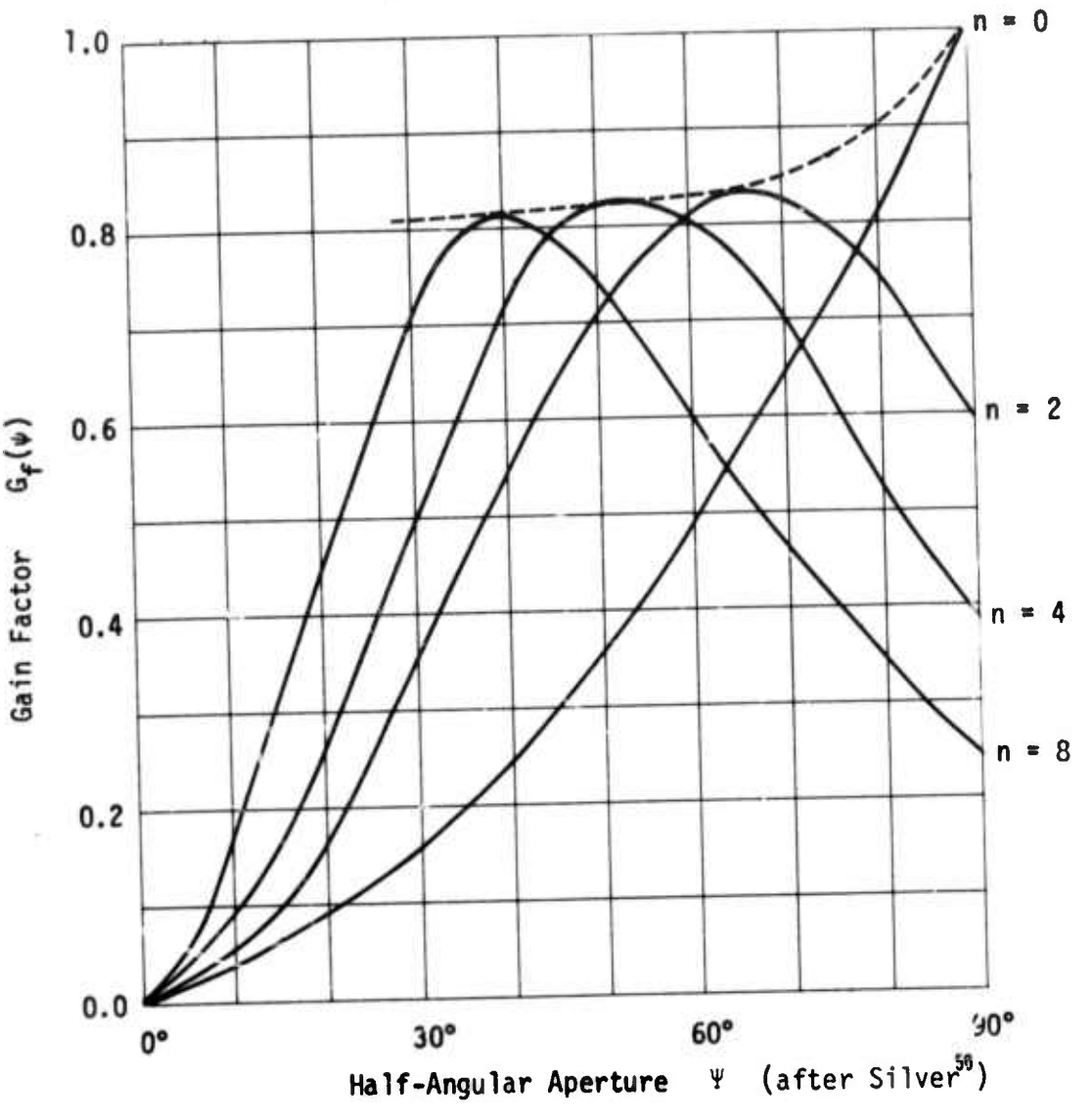


Figure 16. Coupling Aperture Efficiency for Cosinusoidal Distributions

(n > 0); however, an optimum collecting aperture exists for the source distribution. For example, a dipolar field (n=2) shows that the optimum gain factor is reduced by 0.17 and the collecting aperture intercepts only 0.83 of the total available power. The corresponding angular aperture is 64°, and thus a telescope f/d = 0.5 illustrates optimum efficiency. A dipolar source corresponding to the lowest order spherical mode as the directivity of the source is increased (n = 2, 4 . . .). The half angular aperture for maximum coupling decreases; that is, f/d decreases. It is more convenient

to preserve an approximate isotropic source and accommodate a variable f/d ratio by changing an immersion lens focal length. (see Figure 24)

The cosinusoidal distribution has been employed in Figure 16 as representative of the field distribution contained within the dielectric waveguide (see Section A, 3). Another method to express coupling efficiency is by the use of the overlap integral of the actual fields corresponding to the waveguide and the fields produced by the collecting aperture. In this case the distribution of each must have the same width and the same functional dependence to maximize the efficiency. Laboratory experiments have demonstrated that diffraction coupling through an immersion lens can yield efficiency in excess of 0.7, and in some special cases an efficiency in excess of 0.85.

The above discussion is appropriate when the dielectric waveguide dimensions are sufficiently small to restrict the field distribution to the lowest order mode. In this case errors of signal and local oscillator alignment result in a decrease of efficiency due to reduction of the overlap. When the dielectric waveguide will support additional higher-order modes, errors of alignment result in higher-order distributions and a reduction of coupling efficiency to a common mode. Maximum detector response occurs when both signal and local oscillator are excited as the same mode order. The use of even and odd distributions produces zero response and higher-order distributions lead to substantially reduced sensitivity.

## B. TRAVELING-WAVE HETERODYNE DETECTOR PROCESSING TECHNOLOGY

The preceding design analysis has set forth the necessary materials, structure and dimensions for a traveling-wave heterodyne detector configured to employ planar processes. A portion of the experimental effort has been devoted to the demonstration of the traveling-wave concept as a means to achieve wide band heterodyne detection, while another portion of this effort has been devoted to the realization of the necessary material-structure. Specifically, Au-doped, Sb-compensated Ge thin films on a high resistivity GaAs substrate have been considered which can be defined as rectangular dielectric image line waveguides surrounded by a parallel conductor signal transmission line which also serves as photoconductive bias electrodes. The fabrication of various device formats has required the development of several new processing techniques and the refinement of established methods uniquely appropriate for the selected approach. The following sections delineate the pertinent material, characterization and technology consequences. The more conventional, standard processing techniques are not included.

The infrared waveguide transverse cross-section dimensions are in the micron regime. They provide a high degree of field containment and a short carrier transit time. The infrared waveguide longitudinal dimension required is on the order of 5 cm to achieve a high quantum efficiency in the 10 micron region with the limited absorption (see Figure 1).

Compensation is necessary to achieve a minimum carrier lifetime for fast response. A critical doping requirement arises because of the limited Au solubility ($2 \times 10^{16}$ cm$^{-3}$)[32] which simultaneously requires that the Sb concentration also be limited even though the solubility is considerably higher ($10^{19}$ cm$^{-3}$). Failure to maximize the Au concentration and limit the Sb compensation to

$$N_a(\text{Au}) \geq N_d(\text{Sb}) \tag{84}$$

simultaneously compromises the high frequency response or the detector responsivity (see Figure 11). The preferred tolerance upon the approach to equality of doping concentrations is within a factor of two. This

condition is dufficult due to the large differences of diffusion coefficient[46] (Au = $10^{-9}$ $cm^2$/sec @ 830°C and Sb = 5 x $10^{-11}$ $cm^2$/sec @ 830°C) and the limitation imposed by solubility. Homogeneity of these parameters throu[illegible] the optical waveguide longitudinal dimension of 5 cm is also essential.

Another type of processing problem arises through the photolithography because of the requirement for continuous smooth waveguide edges to minimize scattering. The five centimeter dimension for a single continuous uniform image and for a single continuous substrate is significantly larger than the current corresponding electronic integrated circuit technology.

1. Source Material

Germanium was procured from two sources in two configurations, Czochralski-grown Ge with Au doping to the solubility limit with Sb compensation over a magnitude range less than this level, and boat-grown zone-refined Ge with only Sb compensation at the corresponding same concentration levels, separated over an order of magnitude. These materials were characterized by Hall effect measurements at cryogenic and room temperatures, resistivity measurements using a four-point probe, and type testing utilizing a hot-point probe. Surface preparation techniques were developed for the resistivity measurements to provide reproducible results. The method employed sequential lapping using diminishing particle size compounds followed by polishing using fumed silica in an aqueous suspension.

Resistivity measurements of the Czochralski-grown Ge indicated an order of magnitude variation in the radial direction with a substantial uniformity in the axial direction. Metallic Au precipitates were evident near the exterior surface. This inhomogeneity of the Au doping level required slicing of the ingot (1 mm thick) and a rediffusion of Au to achieve uniformity. Outdiffusion of Sb during this Au indiffusion was neglected because of the substantial difference of diffusion coefficient. A similar problem was encountered with the boat-grown Ge relative to the Sb concentration as determined by Hall mobility measurements. This latter material also required Au indiffusion. The Au diffusion was performed in a uniform profile furnace adjusted to 800°C using a flowing Ar atmosphere. The diffusion time was adjusted to provide reasonable uniformity throughout the 1.5 mm thickness, requiring on the order of 70 hours.

For the Au indiffusion thin films of high purity were deposited upon the surface. An electroless plating from an AuCl solution provided high-density films which exhibited poor adhesion during the ensuing diffusion cycle, causing an inhomogeneous concentration. It was found that a high vacuum evaporation yielded the desired adhesion homogeneity using thicknesses of 2,000 Å.

After the Au diffusions were performed, the residual Au film was removed by lapping and polishing prior to characterization. Various slices exhibited an indefinite type conversion from an initial n-type of the Sb-compensated Ge to the p-type representative of Au:Sb-doped Ge. Individual slices were further processed by applying ohmic contacts existing of evaporated In thin films and alloying. To achieve ohmic characteristics the contacting material also contained Sb, Hg, Ga and Tl in addition to the evaporated thin film of In to obtain a suitable cryogenic contact. The I-V characteristics were measured and correlated with bulk resistivity. Photoconduction at 77°K due to infrared illumination served as the final step for characterizing of the source material and subsequent Au diffusion.

## 2. Detector Structure

As a means to verify the traveling-wave concept independent of thin-film structures and questionable doping levels, compensation and contamination, some of these Au:Sb-doped Ge slices were cut into long thin bars with cross sections of 200 x 800, 500 x 800, and 800 x1000μ, all of which had a longitudinal dimension greater than 5 cm. These bars were mounted in a cryogenic Dewar on a cold finger illustrated in Figure 17. A ZnSe immersion lens is employed for the thin waveguide sections. It has been removed in Figure 17. The bar is clamped to provide the signal transmission line. A matching termination resistor is attached at one end and a coaxial transmission line at the other to exit the Dewar. The transformer coupling which appears in Figure 17 has not been employed for the wide band experiments. Evaluation of the traveling-wave structure has demonstrated a base band frequency response in excess of 1 GHz.

The final thin-film photoconductive traveling-wave device structure employs a rectangular dielectric image line waveguide located between the

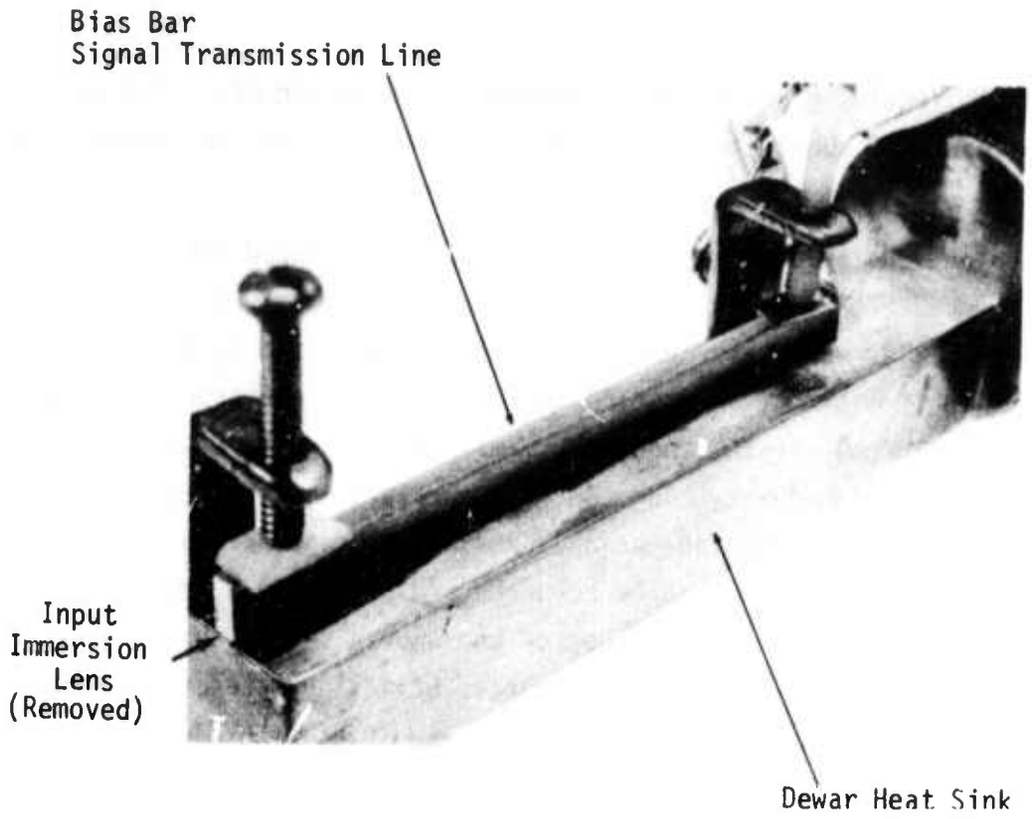


Figure 17. Traveling-Wave Photoconductive Heterodyne Detector Employing Ge Rectangular Bar 200 x 800 Microns x 4.5 cm

slot transmission line or within the strip transmission line as illustrated in the insert of Figure 2. Most of the photolithographic effort has concentrated upon the slot configuration. Several approaches for the thin-film deposition were investigated which differ by the techniques employed and the sequence of development.

Initially, an electron beam evaporation system was modified to allow the rapid evaporation of a Ge:Au/Sb charge within a short time. Previous experiments[3] with such a system indicated that the doping levels of Sb and Ge could be duplicated in a thin-film deposition upon various substrates. These films were typically on the order of 5000 - 6000 Å and exhibited the necessary properties for detector applications. The photoconductive traveling-wave detector design indicates that approximately three microns is preferred for field containment on semi-insulating GaAs (see Figure 6). During the attempt to evaporate such a relatively thick film, segregation of Sb and Au was observed with inhomogeneous distribution of these species. Characterization of the Ge films indicated that predominantly n-type behavior

was present, requiring additional Au doping to be performed. This was precluded by the GaAs substrate because decomposition of GaAs is encountered at 500°C.

A conventional vacuum evaporation system was equipped with a flash evaporation source. This method was deemed to be particularly attractive because previously similar materials were successfully evaporated in the thickness range of 1 to 10 microns, indicating that nearly bulk electronic properties were achieved in polycrystalline thin films. A flash evaporation source was constructed from high-purity tungsten. Temperature elevation to approximately 1100°C is required for Ge evaporation. During the evaporation process alloying of the Ge with the source occurred, resulting in a thin film with electronic properties resembling that of the source rather than the desired Ge:Au/Sb. Attempts to prepare flash sources utilizing materials compatible with Ge were unsuccessful. Attempts to use crucibles with alumina coatings yielded similar results due to microcracks in the coating.

Another procedure investigated employed an RF/DC sputtering system. Because the target diameter is six inches, it was necessary to fabricate a target composed of the procured Ge ingots with Au doping and Sb compensation by slicing and using a "shingle" type mosaic construction. An argon atmosphere was employed. Thin (1 - 3 microns) Ge films deposited by sputtering on various substrates such as glass and GaAs exhibited good adhesion. Characterization of these films revealed that n-type impurities were predominant. To increase the Au concentration, additional metallic Au was deposited as stripes on the shingled target and adjusted by the area of stripes. A number of Ge thin films deposited upon GaAs substrates prepared in this latter fashion were characterized. The majority of specimens were predominantly n-type with some films exhibiting p-type conduction. Characterization of the p-type films at 77°K with $CO_2$ radiation exhibited only trivial photoconductivity. Continuing effort using both of these specimens providing for Au indiffusion generally lead to detachment of the thin film from the substrate due to dissimilar linear thermal expansion properties cycling between 77°K and 800°K. As a result of this detachment and yield problem, further attempts to prepare thin-film structures by sputtering were discontinued.

The metalorganic chemical-vapor deposition epitaxial process has been developed at Rockwell for the IV, III-V and II-VI semiconductors over the

past decade.[47] The metalorganic chemical-vapor deposition apparatus is illustrated in the schematic of Figure 18, indicating the metalorganics for Ga and Al and the gases to introduce As, P, Se, and S. This process leads to a relatively low deposition temperature. The deposition system consists of a vertical quartz tube which forms the reactor chamber containing the silicon carbide coated carbon pedestal which is inductively heated and simultaneously rotated to obtain uniform coverage over the entire area. The system accommodates substrates up to 6 cm diameter. The metalorganic constituents and

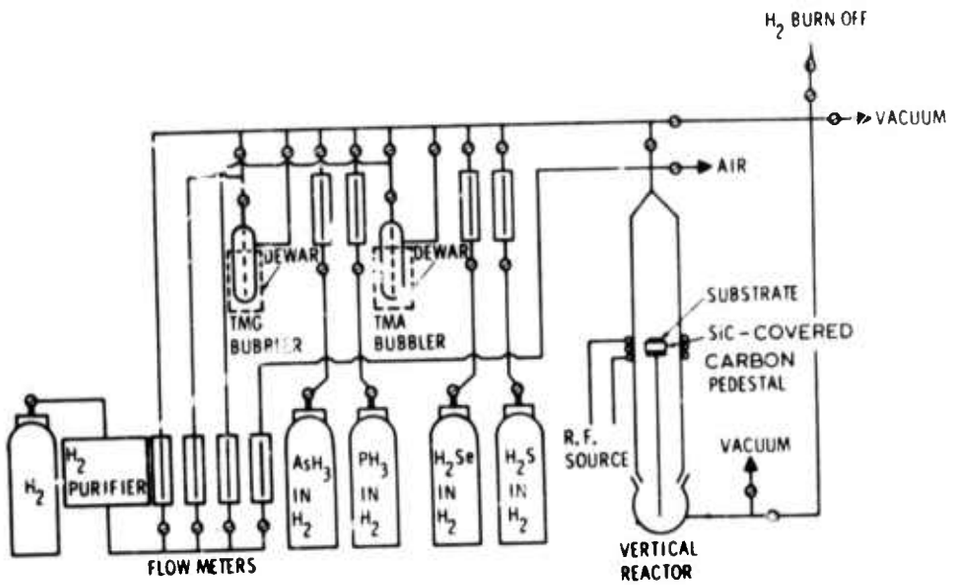


Figure 18. Schematic of Chemical-Vapor Deposition Apparatus

dopants are introduced into the reactor by bubbling the $H_2$ carrier gas through the appropriate liquids available in the form of hydrides. To facilitate the evaluation of heteroepitaxial deposits, single crystal $Al_2O_3$ is also employed as a substrate during each deposition for composition optimization.

The heteroepitaxial deposition of Ge thin films by CVD on GaAs for this application requires the introduction of Au and Sb dopants during the growth cycle. Antimony is available for this purpose in a metalorganic compound. An appropriate source for Au doping useable at the reaction temperatures was not found. As a consequence, it was decided to reverse the procedure whereby Ge having the appropriate Au and Sb concentrations served as the substrate

for the CVD deposition of GaAs. Gallium arsenide was deposited to a thickness of approximately 1 mm in single crystal form. This relatively thick GaAs layer would thus subsequently become the substrate by appropriately reducing the thickness of the Ge to a few microns by standard chemical-abrasive polishing procedures. Several feasibility experiments were performed indicating that at the growth temperature the Ge with its doping would maintain its original properties without degradation of crystallinity. In the actual experiment the chemical-vapor deposition reactor was modified to accommodate the relatively long processing required to obtain a 1 mm thick GaAs single-crystal deposit. The GaAs deposit was lapped and polished plane parallel to the original Ge surface. The composit structure was then mounted in a inverted configuration and the Ge was lapped and polished to a final thickness of approximately five microns. Characterization of the now thin film Ge:Au/Sb on GaAs substrate indicated that the original material properties were maintained without degradation.

## C. TRAVELING-WAVE HETERODYNE DETECTOR PERFORMANCE EXPERIMENTS

Characterization of the traveling-wave photoconductive detectors has encompassed both base band detection and heterodyne operation. The photoconductive response of both bulk elements and thin-film structures has been employed to characterize the Au concentration and Sb compensation doping levels. These conventional techniques will not be delineated herein. Heterodyne operation, both as lumped-element and traveling-wave structures, has been performed using two differentially swept $CO_2$ capillary waveguide lasers and a mode-locked transverse-excited atmospheric $CO_2$ laser determining both the output time and output frequency response so as to verify the traveling-wave concept.

Two conventional grating-tuned $CO_2$ lasers were employed to determine the infrared spectral response at 9.2 and 10.8 microns. Relative data points from this experiment are indicated in Figure 1 employing detector elements 3 mm long and 5 cm long. The data points in Figure 1 may be interpreted as being representative of quantum efficiency if compared to commercial Au-doped Ge photoconductive and HgCdTe photovoltaic detector published data. This experiment clearly indicates the merits of increasing the detector length to improve the responsivity at the longer wavelength regime.

The apparatus employed to display the sweep frequency response of the heterodyne detector system using two $CO_2$ capillary lasers is illustrated in Figure 19 (contained within the transparent plastic covers). These lasers operate at a comparatively high pressure (300 Torr). The frequency is scanned by piezoelectrically driven Fabry-Perot reflectors in "push-pull" so that they serve as a sweep local oscillator and a sweep frequency signal generator. The Fabry-Perot intracavity length of these lasers is 16 cm. The demountable Dewar for the traveling-wave heterodyne detector is illustrated in Figure 20 which contains the cold finger and structure illustrated in Figure 17, using an ultrawide band amplifier (.05 - 1.3 GHz) and a sweep spectrum analyzer. The spectral response of the traveling-wave heterodyne detector is shown in Figure 21. This figure indicates a 3 dB bandwidth of 200 MHz with some response out to 350. The base line markers are 0, 50, and 300 MHz. The detector was connected as a traveling-wave structure. Subsequent measurement have shown that the data of Figure 21 is representative of the sweep laser mode width rather than being indicative of the

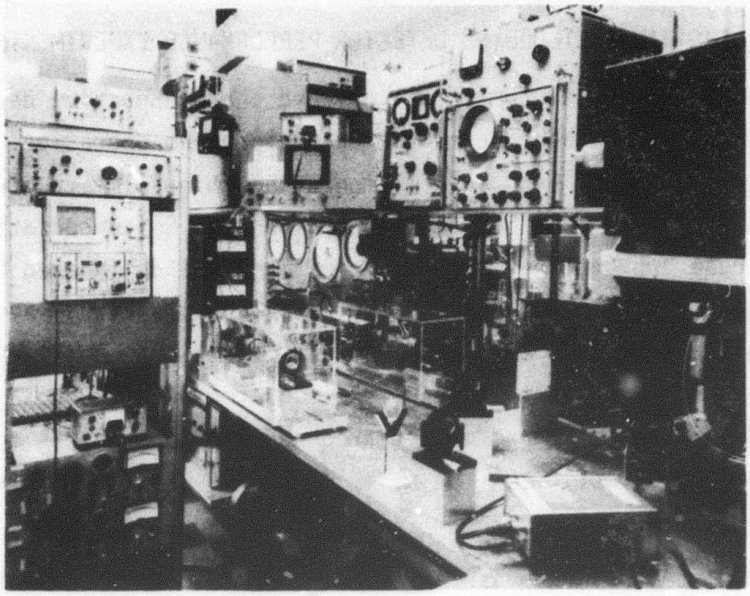

Figure 19. Section of Integrated Optics Laboratory Showing $CO_2$ Capillary Waveguide Lasers, Heterodyne Detector Assembly (Right), and Spectrum Analyzer (Left)

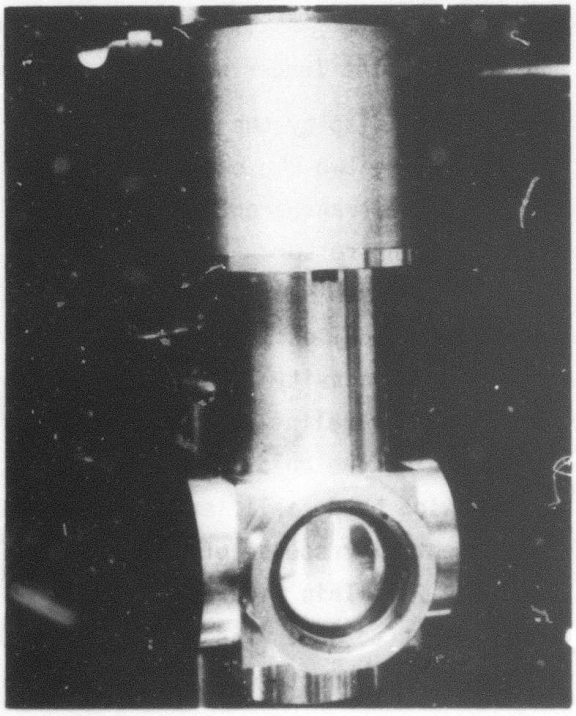

Figure 20. Demountable Dewar for Traveling-Wave Heterodyne Detector

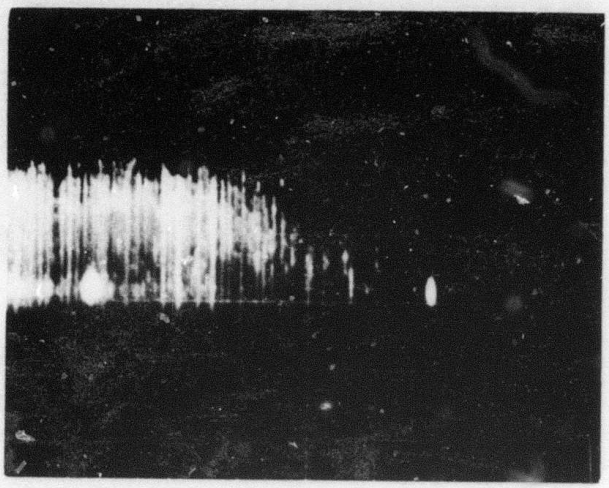

Figure 21. Base Band Frequency Response of Traveling-Wave Heterodyne Photoconductive Detector with Markers at 0, 50 and 200 MHz as Obtained From Two Sweeping $CO_2$ Capillary Lasers

detector performance. The response between 200 and 350 MHz is believed to be more representative of the laser sweep width duty cycle rather than the detector response.

A high-power transverse-excited atmospheric $CO_2$ laser with a grating for tuning of the rotational-vibrational lines and with a low-pressure discharge chamber to prevent mode locking has been employed to further characterize the traveling-wave detector. This laser has been employed in a self-mode-locked configuration without the low-pressure discharge cell. The time response of two traveling-wave detectors is indicated in Figure 22 using single sweeps and an oscilloscope with real time bandwidth of 500 MHz. The time response of this display should produce 0.8 ns rise time. The observed pulsewidth is approximately 2 ns. This type of measurement is also inconclusive.

Another technique employed to determine the bandwidth is based upon the heterodyne interaction of the various longitudinal modes of the TEA self locked $CO_2$ laser. The frequency spacing of the longitudinal modes in this laser is 75 MHz. A narrow band sweep spectrum analyzer covering the entire

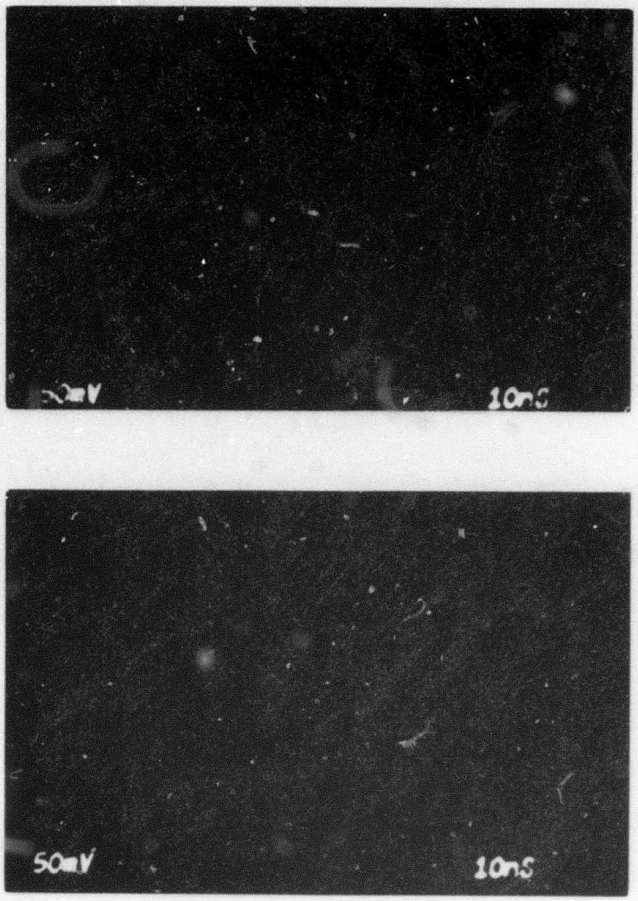


Figure 22. Base Band Time Response of Traveling-Wave Photoconductive Detector to Self Mode Locked TEA $CO_2$ Laser (Pulsewidth $\sim$ 2 ns)

range between .001 and 1.8 GHz with a resolution of 3 MHz has been employed to detect heterodyne interaction between the longitudinal modes. Three results for different traveling-wave heterodyne detectors are illustrated in Figure 23. These figures show a response to 15, 15 and 12 longitudinal modes which correspond to bandwidth of 1125 and 900 MHz. The amplitude fluctuations are due to the comparatively rapid sweep and low repitition TEA $CO_2$ laser repitition rate (3/sec). It is concluded that this latter data confirms the wide band performance of the traveling-wave structure in so far as the available instrumentation permits. Removal of the transmission line termination resistor so that the detector functions as a lumped element reduces the frequency response determined by the capacity loading.

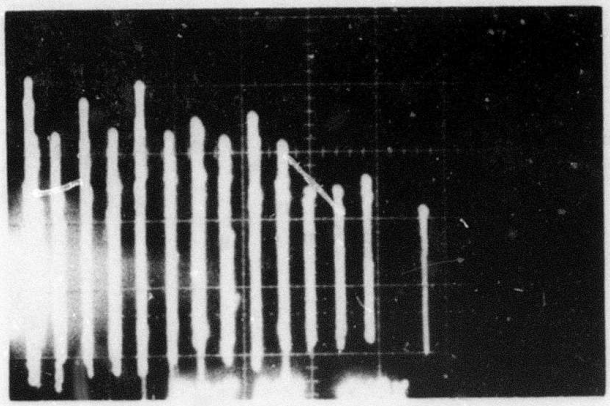

(a) Self Mode Lock of 15 Longitudinal Modes

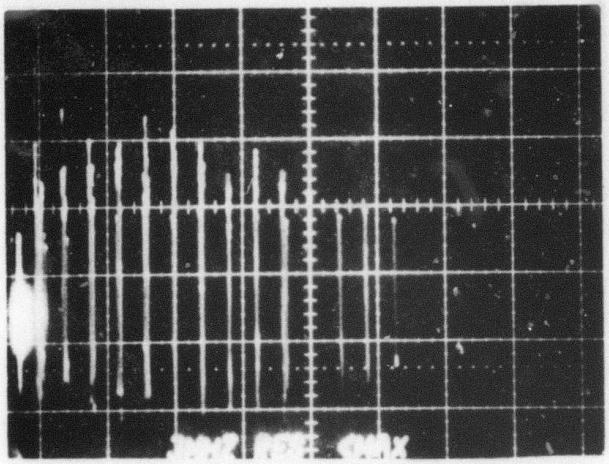

(b) Self Mode Lock of 15 Longitudinal Modes

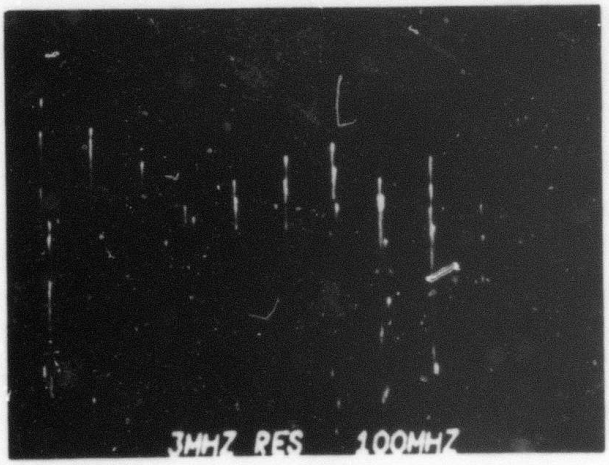


(c) Self Mode Lock of 12 Longitudinal Modes

**Figure** 23. Three Traveling-Wave Heterodyne Spectral Responses to Self Mode Locked TEA $CO_2$ Laser

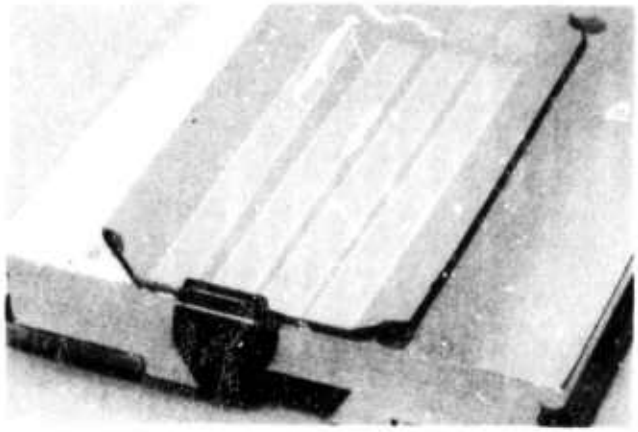

Figure 24. Slot Signal Transmission Line Photolithography on Au-Doped Sb-Compensated Ge Thin Film on GaAs Substrate Mounted with ZnSe Input Coupling Cylindrical Immersion Lens

The response of a $CO_2$ heterodyne receiver with a traveling-wave detector and a wide band IF amplifier has been determined comparing favorably with the theory developed. The IF amplifier bandwidth employed extends from 0.005 to 1.5 Ghz. It has a noise figure of 8.5 dB. Using a coupling efficiency of 0.7 and a tangential signal-to-noise ratio (8 dB), the response of the receiver approaches the calculated values in Table IV within 6 dB. This result is representative of an oversized waveguide with transverse dimensions of 200 x 800 microns where some confidence exists relative to the Au and Sb doping levels and the homogeneity throughout the traveling-wave structure. Generally, smaller waveguide cross sections indicate a considerable uncertainty as to whether the doping levels and relative concentrations were achieved as indicated by reduced base band spectral response width.

The technique of coupling to thin-film waveguides using an immersion lens is illustrated in Figure 24. Generally, the losses of the bias electrodes appear to dominate the performance. Some experiments were performed using Ge fibers approximately 125 microns in diameter. The achievement of identical mode patterns for both the signal and local oscillator propagating through 15 cm of the Ge fibers proved to be a difficult problem subject to mechanical position.

# III. REVIEW

## A. CONCLUSIONS

The effort reported herein has contributed to the far infrared technology by demonstrating that the traveling-wave concept may be applied to extrinsic photoconductive heterodyne detection to obtain wide base band frequency response. The initial phase of this effort[3] has considered various infrared waveguide structures, materials, and compatible processes, together with a hybrid approach to coupling between waveguides through the substrate. A companion effort[6] has addressed traveling-wave electrooptic interactions for phase modulation and surface elastooptic interactions for a frequency shifter to complement the other functional requirements of $CO_2$ laser systems all implemented in an integrated optics format.

The current effort has been addressed to Ge with Au as a dopant to achieve operation at 77°K and with Sb for compensation to obtain fast response. Experiments have demonstrated that alteration of the conventional bulk lumped-element detector design by increasing its length and reducing its transverse cross section can lead to improved quantum efficiency in the spectral regime corresponding to $CO_2$ lasers. This structure leads to a substantial increase of the shunt capacity which, when distributed as in a matched transmission line, can lead to a substantial increase of the bandwidth. The experiments of this effort have demonstrated that the traveling-wave concept yields a bandwidth of at least 1 GHz. Both the slot and strip signal transmission line structures were investigated. The optimum transverse infrared waveguide dimensions are in the 10 - 100 micron range. Smaller transmission line dimensions lead to excessive losses and larger dimensions lead to excessive local oscillator power requirements.

The analysis of the traveling-wave heterodyne detector structure includes the waveguides and phase matching; carrier excitation, lifetime, and diffusion; and detector performance. The analysis of the traveling-wave structure shows that its intrinsic bandwidth extends through the microwave range; however, the requirement to minimize the carrier lifetime to the extent to which this can be achieved becomes a more restrictive limit of the response time rather than the optical-electrical circuit. The limited solubility of Au in Ge and the requirement that the Sb concentration be less than that of Au to minimize

carrier lifetime without compromising the extrinsic absorption places a requirement upon the materials-processes which has proven to be difficult in its realization simultaneously in a thin-film structure. Further development of processes to satisfy this requirement reproducibly is required in order to take advantage of the traveling-wave concept applied in an integrated optics format.

The responsivity performance of a photoconductive heterodyne detector in an integrated optics format is comparable to current lumped-element devices except for the advantageous effect of the longer absorption length upon the spectral response. Any coupling inefficiency allowed has a direct degradation upon the receiver system sensitivity. The alignment of the local oscillator is critical because the same transverse mode, kind, and order must be realized as employed for the signal. Restriction to the lowest order can partially alleviate the alignment sensitivity at the expense of additional local oscillator power.

The requirement of a cryogenic environment for photodetectors achieved in a Dewar negates the advantage of an integrated optics approach justified by size and weight. Dewars designed specifically for this purpose are desirable, and further, it may prove feasible to include additional integrated optical circuits such as frequency shifters, modulators and couplers where the cryogenic environment may improve the efficiency and reduce the loss.

## B. ACKNOWLEDGEMENTS

Sincere appreciation is expressed for the heteroepitaxy chemical deposition by Dr. H. M. Manasevit, together with Mr. W. I. Simpson; the RF sputtered and evaporated deposition, together with most of the photolithographic processing, due to Mr. J. E. Coker, electron microscopy by Mr. R. E. Johnson and the chemo-mechanical polishing by Mr. G. W. Johnson.

## C. REFERENCES

1. S. E. Miller, E. A. J. Marcatili and T. Li, "Research Towards Optical-Fiber Transmission Systems," Proc. IEEE 61, 1703 (1973).
2. C. M. Stickley, D. Albares, H. F. Taylor and T. G. Giallorenzi, "Anticipated Uses of Fiber and Integrated Optics in the Defense Department," OSA Topical Meeting on Integrated Optics, New Orleans, Jan. 1974.
3. D. B. Anderson, et.al., "Hybrid Waveguides, Integrated Optics for 10 Micron Wavelengths," Rockwell International Interim Technical Reports C73-291.2/.4/.6/501, June 29, September 30, December 31, 1975, N00014-73-C-0297.

4. J. T. Boyd and D. B. Anderson, "Radiation of End-Fire Optical Waveguide Coupler," Optics Comm. 13, 353 (1975).
5. D. B. Anderson, et.al., "Hybrid Waveguides, Integrated Optics for 10 Micron Wavelengths," Rockwell International Interim Technical Reports C73-291.8/.10/501, March 30, June 30, 1975, N00014-73-C-0297
6. D. B. Anderson, et.al., "Integrated Optical Modulators for 10 Micron Wavelengths," Rockwell International Final Technical Report C73-293.14/501, March 17, 1975, N00014-73-C-0271.
7. J. D. McMullen, D. B. Anderson, R. L. Davis, "Optical-Gain in CW Transverse Discharge Transverse-Gas-Flow $CO_2$:$N_2$:He Planar-Waveguide Laser," J. Appl. Phys. 45, 5084 (1974).
8. J. D. McMullen, R. L. Davis, "Tunable 10 Micron Laser, An Integrated Optics Approach to Infrared Gas Lasers," Rockwell International Report C72-650.21/501, Feb 28, 1974, N00014-72-C-0505.
9. R. W. Ralston, J. N. Walpole, T. C. Harman, I. Melngailis, "Double Heterostructure $Pb_{1-x}Sn_xTe$ Waveguide at 10.6 μ," Appl. Phys. Lett. 26, 64 (1975).
10. E. M. Logothetis, H. Holloway, A. J. Varga and E. Wilkes, "Infrared Detection by Schottky Barriers in Epitaxial PbTe," Appl. Phys. Lett. 19, 381 (1971).
11. J. P. Donnelly and H. Holloway, "Photodiodes Fabricated in Epitaxial PbTe by $Sb^+$ Ion Implantation," Appl. Phys. Lett. 23, 682 (1973).
12. D. L. Spears, "Planar HgCdTe Quadrantal Arrays for Gigahertz Heterodyne Operation at 10.6 μm," Lincoln Laboratory MIT Report ESD-TR-75-118, Sol. St. Research, April 1975.
13. C. B. Shaw and C. Warner, III, "Variational Approximation to the Dominant Propagation Constants of Rectangular Dielectric Waveguides," Bull. Am. Phys. Soc. 12, 887 (1967).
14. W. Schlosser and H. G. Unger, "Partially Filled Waveguides and Surface Waveguides of Rectangular Cross Section," Advances in Microwaves Vol. 1, L. Young, Editor, Academic Press, 1966.
15. J. E. Goell, "A Circular-Harmonic Computer Analysis of Rectangular Dielectric Waveguides," BSTJ 48, 2133 (1969).
16. S. B. Cohn, "Slot Line on a Dielectric Substrate," IEEE Trans. MTT 17, 768 (1969).
17. S. Wang, Solid-State Electronics, McGraw-Hill Book Company, 1966.
18. S. M. Sze, Physics of Semiconductor Devices, John Wiley and Sons, Inc., 1969.

19. R. A. Smith, Semiconductors, Cambridge University Press, 1961.
20. M. DiDomenico and O. Svelto, "Solid-State Photodetection: A Comparison Between Photodiodes and Photoconductors," Proc. IEEE 52, 136 (1964).
21. R. H. Bube, Photoconductivity of Solids, John Wiley and Sons, Inc., 1960.
22. W. C. Johnson, Transmission Lines and Networks, McGraw-Hill Book Co., New York, 1950.
23. R. E. Collin, Field Theory of Guided Waves, McGraw-Hill Book Co., New York, 1960.
24. W. H. Louisell, Coupled Mode and Parametric Electronics, Wiley, 1960.
25. F. R. Arams, E. W. Sard, B. J. Peyton and F. P. Pace, IEEE JQE-3, 484 (1967).
26. A. Yariv, Introduction to Optical Electronics, Holt, Rinehart and Winston, Inc., 1971.
27. M. C. Teich, "Coherent Detection in the Infrared," In Semiconductors and Semimetals, Vol. 5, Academic Press, 1970.
28. J. I. Pankove, Optical Processes in Semiconductors, Prentice-Hall, Inc., 1971.
29. T. S. Moss, G. J. Burrell and B. Ellis, Semiconductor Opto-Electronics, John Wiley and Sons, Inc., 1973.
30. T. P. Vogl, J. R. Hansen and M. Garbuny, "Photoconductive Time Constants and Related Characteristics of p-type Gold-Doped Germanium," J. Opt. Soc. Amer. 51, 70 (1961).
31. B. I. Boltaks, Diffusion in Semiconductors, Academic Press, 1963.
32. F. A. Trumbore, "Solid Solubilities of Impurity Elements in Germanium and Silicon," BSTJ 39, 205 (1960).
33. L. Johnson and H. Levinstein, "Infrared Properties of Gold in Germanium," Phys. Rev. 117, 1191 (1960).
34. D. Marcuse, Theory of Dielectric Optical Waveguides, Academic Press, 1974.
35. T. Takano and J. Hamasaki, "Propagating Modes of a Metal-Clad-Dielectric-Slab Waveguide for Integrated Optics," IEEE J. Quantum Elec. QE-8, 206 1972.
36. A. Reisinger, "Characteristics of Optical Guided Modes in Lossy Waveguides," Appl. Opt. 12, 1015 (1973).
37. I. P. Kaminow, W. L. Mammel and H. P Weber, "Metal-Clad Optical Waveguides: Analytical and Experimental Study," Appl. Opt. 13, 396 (1974).

38. T. E. Batchman and S. C. Rashleigh, "Mode-Selective Properties of a Metal-Clad-Dielectric-Slab Waveguide for Integrated Optics," IEEE J. Quantum Elec. QE-8, 848 (1972).

39. E. M. Garmire and H. Stoll, "Propagation Losses in Metal-Film-Substrate Optical Waveguides," IEEE J Quantum Elec. QE-8, 763 (1972).

40. F. R. Arams, E. W. Sard, B. J. Peyton and F. P. Pace, "Infrared Heterodyne Detection with Gigahertz IF Response," Semiconductors and Semimetals, 5, Academic Press, New York, 1970.

41. H. Melchoir, M. B. Fisher, and F. R. Arams, "Photodetectors for Optical Communication Systems," Proc. of IEEE, 58 (1970).

42. M. C. Teich, "Infrared Heterodyne Detection," Proc. IEEE 56, 37 (1968).

43. B. J. Peyton, A. J. DiNardo, G. M. Kanischak, F. R. Arams, R. A. Lange and E. W. Sard, "High-Sensitivity Receiver for Infrared Laser Communications," IEEE JQE QE-8, 252 (1972).

44. J. J. Degnan and B. J. Klein, "Optical Antenna Gain. 2: Receiving Antennas," Appl. Optics 13, 2397 (1974).

45. S. C. Cohen, "Heterodyne Detection: Phase Front Alignment, Beam Spot Size and Detector Uniformity," Appl. Optics 14, 1953 (1975).

46. W. C. Dunlap, "Gold as an Acceptor in Germanium," Phys. Rev. 97, 614 (1955).

47. H. M. Manasevit, et. al., "The Use of Metal-Organics in the Preparation of Semiconductor Materials, -I Epitaxial Ga-V, -II, II-VI Compounds, -III Studies of Epitaxial, III-V Al Compound Formation Using Trimethylaluminum, -IV The Nitrides of Al and Ga," J. of Electrochemical Soc. 116, 1725 (1969); 118, 664, 647, 1864 (1971).

48. R. C. Hansen, Microwave Scanning Antennas, Vol. I, Academic Press, 1964.

49. L. C. Martin, The Theory of the Microscope, American Elsevier, 1966.

50. S. Silver, Microwave Antenna Theory and Design, McGraw-Hill Book Company, Inc., 1949, Chapter 12.